CMS Physics Analysis Summary

Contact: cms-pag-conveners-higgs@cern.ch 2021/10/16

Constraints on anomalous Higgs boson couplings to vector bosons and fermions in its production with associated particles using the $H \to \tau\tau$ final state.

The CMS Collaboration

Abstract

A study of anomalous couplings of the Higgs boson to vector bosons and fermions is presented. The data were recorded by the CMS experiment at a center-of-mass energy of 13 TeV and correspond to an integrated luminosity of 138 fb^{-1}. The study uses Higgs boson candidates produced mainly in electroweak vector boson or gluon fusion that subsequently decay to a pair of τ leptons. Matrix element and multivariate techniques were employed in a search for anomalous effects. The results are combined with those from the $H \to 4l$ and $H \to \gamma\gamma$ decay channels to yield the most stringent constraints on anomalous Higgs boson couplings to date.

1 Introduction

The discovery of the Higgs boson (H) by the ATLAS and CMS experiments at the LHC [1–3] has opened a new era for particle physics, where the characterization of the new boson is of crucial importance. Studies of the H test the standard model (SM) and probe for new physics. Thus far, the properties of the H are found to be consistent with the SM [4–10]. In particular, nonzero spin assignments of the H have been excluded [11, 12], and its spin-parity quantum numbers are consistent with $J^{PC} = 0^{++}$ [1–3, 11, 13–21]. However, the limited precision of current studies allows small anomalous couplings of the H to two electroweak gauge bosons. Possible *CP*-violating effects in H couplings to fermions (Hff) have been constrained by the CMS and ATLAS Collaborations in $\mathrm{t\bar{t}H}$ production [21–23], where *CP*-odd couplings may appear at tree level, and are not suppressed by loop effects. In the SM, the coupling of the H to gluons (Hgg) is mediated via loops, where the top quark dominates. Any observed *CP* violation in the Hgg interaction would indicate either a *CP*-odd Htt coupling or a new effective interaction requiring new particles. Thus, a study of the Hgg coupling provides complementary information on the nature of the H and serves as an indirect search for new phenomena. Both CMS and ATLAS Collaborations have previously searched for *CP*-violation in the Hgg coupling [20, 21], but the current constraints are quite weak; slightly below the 1σ level.

In this note, we report on a search for anomalous effects, including possible signs of *CP* violation, in the tensor structure of the H interactions with electroweak bosons (HVV) and gluons (Hgg) in the production of the H. We follow the formalism used in previous CMS studies of anomalous couplings in Run 1 and Run 2, described in Refs. [11, 14–19, 21, 22]. The two dominant production channels employed in this study are electroweak vector boson fusion, VBF, and gluon fusion, ggH. Compared to our previous study in the $\mathrm{H} \to \tau\tau$ final state [19], we have improved the sensitivity to anomalous effects with multivariate tools, optimization of the final state categorization, and an increased data sample. The analysis utilizes a matrix element likelihood approach (MELA) [13, 24–27] and a neural network [28] to optimize the measurement of anomalous couplings using production and decay kinematic information. Compared to our similar study in the $\mathrm{H} \to 4\ell$ final state [21], where ℓ denotes an electron or muon and both production and decay information is used, the inclusion of the $\mathrm{H} \to \tau\tau$ final state leads to a substantial improvement in constraints on anomalous couplings due to a larger sample of VBF and ggH events reconstructed in association with two jets. The results obtained from the two decay channels are further combined to form the most stringent constraint on anomalous couplings. The combined ggH results are further combined with the $\mathrm{t\bar{t}H}$ analysis using the $\mathrm{H} \to \gamma\gamma$ and $\mathrm{H} \to 4\ell$ decays [22] under the assumption of top quark dominance in gluon fusion to produce the most stringent limits on the Htt anomalous couplings.

The note is organized as follows. The phenomenology of anomalous HVV and Hff couplings is discussed in Section 2. The kinematics of the processes studied and the observables utilized in this study to search for anomalous contributions are described in Section 3. The data used in this study, the Monte Carlo (MC) simulation, as well as event reconstruction methods are described in Section 4. The event selection and categorization is documented in Section 5. Methods to estimate backgrounds are given in Section 6 and the sources of systematic uncertainty are listed in Section 7. The analyses of the Hgg and HVV interactions using $\mathrm{H} \to \tau\tau$ decays are presented in Sections 8 and 9, respectively. The combination of the $\mathrm{H} \to \tau\tau$ results with the $\mathrm{H} \to 4\ell$ and $\mathrm{H} \to \gamma\gamma$ decay channels is detailed in Section 10. Section 11 summarizes the results.

2 Phenomenology of anomalous couplings and cross sections

In this study we follow the formalism used in the measurement of H couplings in earlier CMS analyses [11, 14–19, 21, 22]. The theoretical approach is described in Refs. [24–27, 29–37].

Anomalous interactions of a spin-0 H with two spin-1 gauge bosons VV, such as WW, ZZ, Zγ, $\gamma\gamma$, and gg, are parameterized by a scattering amplitude that includes three tensor structures with expansion of coefficients up to (q^2/Λ^2)

$$\mathcal{A}(\mathrm{HVV}) \sim \left[a_1^{\mathrm{VV}} + \frac{\kappa_1^{\mathrm{VV}} q_1^2 + \kappa_2^{\mathrm{VV}} q_2^2}{\left(\Lambda_1^{\mathrm{VV}}\right)^2} \right] m_{\mathrm{V1}}^2 \epsilon_{\mathrm{V1}}^* \epsilon_{\mathrm{V2}}^* + a_2^{\mathrm{VV}} f_{\mu\nu}^{*(1)} f^{*(2)\mu\nu} + a_3^{\mathrm{VV}} f_{\mu\nu}^{*(1)} \tilde{f}^{*(2)\mu\nu}, \quad (1)$$

where q_i, ϵ_{Vi}, and m_{V1} are the four-momentum, polarization vector, and pole mass of the gauge boson, indexed by $i = 1, 2$. The gauge boson's field strength tensor and dual field strength tensor are $f^{(i)\mu\nu} = \epsilon_{\mathrm{V}i}^{\mu} q_i^{\nu} - \epsilon_{\mathrm{V}i}^{\nu} q_i^{\mu}$ and $\tilde{f}_{\mu\nu}^{(i)} = \frac{1}{2}\epsilon_{\mu\nu\rho\sigma} f^{(i)\rho\sigma}$. The coupling coefficients a_i^{VV}, which multiply the three tensor structures, and $\kappa_i^{\mathrm{VV}}/(\Lambda_1^{\mathrm{VV}})^2$, which multiply the next term in the q^2 expansion for the first tensor structure, are to be determined from data, where Λ_1 is the scale of beyond the SM (BSM) physics. The convention $\epsilon_{0123} = +1$ defines the relative sign of the CP-odd and CP-even couplings. The sign in front of the gauge fields in the covariant derivative defines the sign of the photon field and sets the sign convention of the Zγ couplings. Both conventions rely on the tools adopted in this analysis and are discussed in Section 4.1.

In Eq. (1), the only nonzero SM contributions at tree level are a_1^{WW} and a_1^{ZZ}, which are assumed to be equal under custodial symmetry. All other ZZ and WW couplings are considered anomalous contributions, which are either due to BSM physics or small contributions arising in the SM from loop effects that cannot be detected with the current precision. Among the anomalous contributions, considerations of symmetry and gauge invariance require $a_1^{\mathrm{Z}\gamma} = a_1^{\gamma\gamma} = a_1^{\mathrm{gg}} = 0$, $\kappa_1^{\mathrm{ZZ}} = \kappa_2^{\mathrm{ZZ}}$, $\kappa_1^{\gamma\gamma} = \kappa_2^{\gamma\gamma} = 0$, $\kappa_1^{\mathrm{gg}} = \kappa_2^{\mathrm{gg}} = 0$, and $\kappa_1^{\mathrm{Z}\gamma} = 0$ [38]. Therefore, in total there are 13 independent parameters that describe the H coupling to the electroweak gauge bosons and two that describe the coupling to gluons. The a_3^{VV} couplings are CP-odd, and their presence together with any other CP-even couplings would result in CP violation in a given process.

Our earlier measurements [11] indicated substantially stronger limits on $a_2^{\gamma\gamma,\mathrm{Z}\gamma}$ and $a_3^{\gamma\gamma,\mathrm{Z}\gamma}$ couplings from $\mathrm{H} \to \mathrm{Z}\gamma$ and $\mathrm{H} \to \gamma\gamma$ decays with on-shell photons than from measurements with virtual photons, so we do not pursue measurements of these parameters in this note, and they are set to zero when measuring other anomalous couplings.

As the event kinematics of the H production in WW fusion and in ZZ fusion are very similar, it is essentially impossible to distinguish between a_i^{WW} and a_i^{ZZ} in the VBF production. It is therefore possible to use different conventions to set the relative size of the HWW and HZZ couplings. The results can be reinterpreted for any chosen relationship between the a_i^{WW} and a_i^{ZZ} couplings [18].

In our measurements we adopt two approaches to set the relationship between the a_i^{WW} and a_i^{ZZ} couplings. In the first approach (Approach 1) they are analyzed together assuming $a_i^{\mathrm{WW}} = a_i^{\mathrm{ZZ}}$ and $\kappa_i^{\mathrm{ZZ}}/(\Lambda_1^{\mathrm{ZZ}})^2 = \kappa_i^{\mathrm{WW}}/(\Lambda_1^{\mathrm{WW}})^2$. In the second approach (Approach 2) we reinterpret the results for the CP-violating coupling a_3 following the procedure described in Ref. [18]. In this reinterpretation we apply additional considerations of custodial and SU(2)×U(1) symmetries in the relationships of anomalous couplings [38, 39]. With $a_2^{\gamma\gamma,\mathrm{Z}\gamma}$ and $a_3^{\gamma\gamma,\mathrm{Z}\gamma}$ fixed to

zero we are left with a simple relationship between a_3^{WW} and a_3^{ZZ},

$$a_3^{WW} = \cos^2\theta_W \, a_3^{ZZ}. \tag{2}$$

It is convenient to measure the effective cross section ratios f_{ai} rather than the anomalous couplings a_i themselves, as most uncertainties cancel in the ratio. Moreover, the effective fractions are conveniently bounded between -1 and 1, independent of the coupling convention. The effective fractional cross sections f_{ai} are defined as follows [21],

$$\begin{aligned}
f_{a3} &= \frac{|a_3|^2\sigma_3}{|a_1|^2\sigma_1 + |a_2|^2\sigma_2 + |a_3|^2\sigma_3 + |\kappa_1|^2\sigma_{\Lambda1} + |\kappa_1^{Z\gamma}|^2\sigma_{\Lambda1}^{Z\gamma}} \operatorname{sgn}\left(\frac{a_3}{a_1}\right), \\
f_{a2} &= \frac{|a_2|^2\sigma_2}{|a_1|^2\sigma_1 + |a_2|^2\sigma_2 + |a_3|^2\sigma_3 + |\kappa_1|^2\sigma_{\Lambda1} + |\kappa_1^{Z\gamma}|^2\sigma_{\Lambda1}^{Z\gamma}} \operatorname{sgn}\left(\frac{a_2}{a_1}\right), \\
f_{\Lambda1} &= \frac{|\kappa_1|^2\sigma_{\Lambda1}}{|a_1|^2\sigma_1 + |a_2|^2\sigma_2 + |a_3|^2\sigma_3 + |\kappa_1|^2\sigma_{\Lambda1} + |\kappa_1^{Z\gamma}|^2\sigma_{\Lambda1}^{Z\gamma}} \operatorname{sgn}\left(\frac{-\kappa_1}{a_1}\right), \\
f_{\Lambda1}^{Z\gamma} &= \frac{|\kappa_2^{Z\gamma}|^2\sigma_{\Lambda1}^{Z\gamma}}{|a_1|^2\sigma_1 + |a_2|^2\sigma_2 + |a_3|^2\sigma_3 + |\kappa_1|^2\sigma_{\Lambda1} + |\kappa_1^{Z\gamma}|^2\sigma_{\Lambda1}^{Z\gamma}} \operatorname{sgn}\left(\frac{-\kappa_2^{Z\gamma}}{a_1}\right),
\end{aligned} \tag{3}$$

where σ_i is the cross section for the process corresponding to $a_i = 1$ with all other couplings set to zero. The choice of the sign for the κ_1 and $\kappa_2^{Z\gamma}$ terms follows the convention introduced in the prior results [11, 17, 18, 21]. The othe sign conventions follow the JHUGEN 7.0.2 event generator as discussed in Section 4.1 and Ref. [40]. For consistency with previous CMS measurements in the $H \to 4\ell$ final state [11, 21], the σ_i coefficients are defined for the $gg \to H \to VV \to 2e2\mu$ process. The numerical values are given in Table 1 as calculated using the JHUGEN 7.0.2 event generator [24–27]. It is assumed that the couplings in Eq. (1) are constant and real, and therefore this formulation is equivalent to an effective Lagrangian formalism.

Table 1: The cross sections for the anomalous contributions used to define the fractional cross sections. All cross sections are given relative to the SM value (σ_1). In the case of the κ_1 and $\kappa_2^{Z\gamma}$ couplings, the numerical values $\Lambda_1 = \Lambda_1^{Z\gamma} = 100\,\text{GeV}$ are considered so as to keep all coefficients of similar order of magnitude.

Fraction	σ_i/σ_1
f_{a3}	0.153
f_{a2}	0.361
$f_{\Lambda1}$	0.682
$f_{\Lambda1}^{Z\gamma}$	1.746

The Hgg coupling is a purely loop-induced process, which in the SM is generated by the top quark, with a smaller contribution from the bottom quark. This interaction is *CP*-even in the SM. However, a contribution of the *CP*-odd interaction in the H coupling to fermions is not ruled out, and the search for such a *CP*-violating interaction can be performed in $t\bar{t}H$ production and $H \to \tau\tau$ decay. Under the assumption that other BSM particles do not contribute to the gluon fusion loop, a *CP* structure measurement in the ggH process is equivalent to the measurement of *CP* structure in Yukawa interactions, which can be parameterized with the amplitude

$$\mathcal{A}(Hff) = -\frac{m_f}{v}\bar{\psi}_f\left(\kappa_f + i\,\tilde{\kappa}_f\gamma_5\right)\psi_f\,. \tag{4}$$

The effective fractional cross section for Hff couplings is defined as [22]

$$f_{\mathrm{CP}}^{\mathrm{Hff}} = \frac{|\widetilde{\kappa}_{\mathrm{f}}|^2}{|\kappa_{\mathrm{f}}|^2 + |\widetilde{\kappa}_{\mathrm{f}}|^2} \,\mathrm{sgn}\left(\frac{\widetilde{\kappa}_{\mathrm{f}}}{\kappa_{\mathrm{f}}}\right) . \tag{5}$$

An equivalent effective mixing angle α^{Hff} is also used to describe the CP-odd contribution to the H Yukawa couplings and is defined as

$$\alpha^{\mathrm{Hff}} = \tan^{-1}\left(\frac{\widetilde{\kappa}_{\mathrm{f}}}{\kappa_{\mathrm{f}}}\right) , \tag{6}$$

where $|f_{\mathrm{CP}}^{\mathrm{Htt}}| = \sin^2\alpha^{\mathrm{Hff}}$. Therefore, with just two contributions to the gluon fusion loop (CP-even and CP-odd fermion couplings), the two parameters are equivalent. However, with consideration of multiple contributions, as discussed in the case of electroweak HVV couplings above, multiple fractional contributions have to be defined and a single angle is not sufficient. The gluon fusion loop can be generated by unknown heavy BSM particles, in addition to the SM fermions, and the effective coupling results in the CP-even a_2^{gg} and CP-odd a_3^{gg} couplings, defined in Eq. (1). In the effective field theory (EFT) approach [39], they correspond to two EFT couplings in the Higgs basis:

$$\begin{aligned} c_{\mathrm{gg}} &= -\frac{1}{2\pi\alpha_{\mathrm{S}}} a_2^{\mathrm{gg}}, \\ \widetilde{c}_{\mathrm{gg}} &= -\frac{1}{2\pi\alpha_{\mathrm{S}}} a_3^{\mathrm{gg}}. \end{aligned} \tag{7}$$

Therefore, there are at least four contributions to consider (κ_{t}, $\widetilde{\kappa}_{\mathrm{t}}$, c_{gg}, $\widetilde{c}_{\mathrm{gg}}$), where in the SM we have (κ_{t}, $\widetilde{\kappa}_{\mathrm{t}}$, c_{gg}, $\widetilde{c}_{\mathrm{gg}}$) = (1, 0, 0, 0). The dependence of the ggH cross section and H branching fractions on these parameters is given in Ref. [40]. Under the assumptions that the only SM particles contributing to the loop are the top and bottom quarks and (κ_{b}, $\widetilde{\kappa}_{\mathrm{b}}$) = (1, 0), the ggH cross section relative to the SM expectation is found to be

$$\begin{aligned} \mu_{\mathrm{ggH}} =& 1.1068\kappa_{\mathrm{t}}^2 + 0.0082 - 0.1150\kappa_{\mathrm{t}} + 2.5717\widetilde{\kappa}_{\mathrm{t}}^2 + 1.0298(12\pi^2 c_{\mathrm{gg}})^2 + 2.3170(8\pi^2\widetilde{c}_{\mathrm{gg}})^2 \\ &+ 2.1357(12\pi^2 c_{\mathrm{gg}})\kappa_{\mathrm{t}} - 0.1109(12\pi^2 c_{\mathrm{gg}}) + 4.8821(8\pi^2\widetilde{c}_{\mathrm{gg}})\widetilde{\kappa}_{\mathrm{t}}. \end{aligned} \tag{8}$$

Within the framework of our analysis, however, it is hard to distinguish between the κ_{f} and a_2^{gg} contributions, or between $\widetilde{\kappa}_{\mathrm{f}}$ and a_3^{gg}. There are small differences in the p_{T} distributions of the H, and one can also observe effects in the off-shell H production [38]. However, the former is too small to have a noticeable effect in this analysis, and the latter is not relevant in our on-shell topology. Therefore, we absorb the SM fermion loop contribution, dominated by the heavy top quark, into the overall a_2^{gg} and a_3^{gg} couplings. The only remaining effective fractional cross section for the Hgg interaction is defined as [21]

$$f_{a3}^{\mathrm{ggH}} = \frac{|a_3^{\mathrm{gg}}|^2}{|a_2^{\mathrm{gg}}|^2 + |a_3^{\mathrm{gg}}|^2} \,\mathrm{sgn}\left(\frac{a_3^{\mathrm{gg}}}{a_2^{\mathrm{gg}}}\right) . \tag{9}$$

Under the assumption that only the top and bottom quarks contribute to gluon fusion with $\kappa_{\mathrm{t}} = \kappa_{\mathrm{b}}$ and $\widetilde{\kappa}_{\mathrm{t}} = \widetilde{\kappa}_{\mathrm{b}}$, the following relationship [38] holds:

$$\left|f_{\mathrm{CP}}^{\mathrm{Htt}}\right| = \left(1 + 2.38\left[\frac{1}{\left|f_{a3}^{\mathrm{ggH}}\right|} - 1\right]\right)^{-1} . \tag{10}$$

In this note, we present a search for anomalous Hgg couplings in the gluon fusion production and anomalous HWW, HZZ, and HZγ (HVV) couplings in VBF H (VBF) and associative H production with a W or a Z boson (VH production). In addition, the Hgg measurement is interpreted in terms of constraints on Hff couplings under the assumption of top quark dominance in gluon fusion. We measure a given anomalous coupling while setting the values of all other anomalous coupling parameters to zero with the exception of measuring the *CP*-sensitive parameters. As *CP* violation in electroweak VBF and VH production modifies the same kinematic distributions as those in the gluon fusion process, we leave both of the *CP*-sensitive parameters f_{a3} and f_{a3}^{ggH} unconstrained. *CP* violation in the decay of the H to a pair of tau leptons does not affect the measurements of the production process, and thus we assume SM kinematics for the H decays.

3 Kinematics in production and discriminants

When combined with the momentum transfers of the vector bosons, the five angles illustrated in Fig. 1 provide complete kinematic information for production and decay of the H. There are

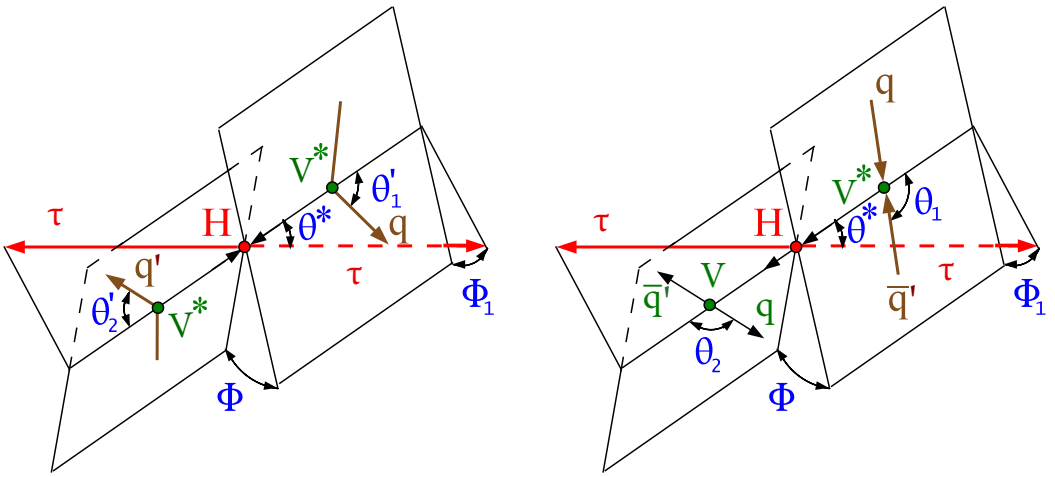

Figure 1: Illustrations of H production in vector boson fusion $qq' \to qq'H$ (left) and $q\bar{q}' \to V^* \to VH$ (right). The decay $H \to \tau\tau$ is shown without illustrating the further decay chain. Angles and invariant masses fully characterize the orientation of the production and two-body decay chain and are defined in the suitable rest frames [24, 26].

four possible and practical ways to access *CP*-violating effects (or more generally anomalous HVV or Hff couplings) using the reconstructed $H \to \tau\tau$ events: i) correlation of two quark jets and leptons in VBF and VH production; ii) correlation of two jets in QCD production of the H (gluon fusion); iii) correlation of quark jets in $t\bar{t}H$ or tH production; and iv) correlation of decay products of two τ leptons. Because exotic non-zero spin assignments of the H have been excluded [11–19, 41–46], we focus on the analysis of couplings of a spin-zero H. There are no spin correlations between the production and decay through a spin-zero object. Therefore, all four of the above processes can be studied independently and they target different parameters that are independent, even though all of them may be related to anomalous effects. This analysis focuses on searching for anomalous effects in the topologies described as the first and second items above. We refer to those as the anomalous HVV and Hgg couplings, respectively.

3.1 Correlation of two quark jets and leptons in VBF and VH production

Kinematic distributions of associated particles in VBF and VH production are sensitive to the quantum numbers and anomalous couplings of the H. A set of observables could be defined in production, such as $\mathbf{\Omega}^{\text{assoc}} = \{\theta_1^{\text{VBF}}, \theta_2^{\text{VBF}}, \theta^{*\text{VBF}}, \Phi^{\text{VBF}}, \Phi_1^{\text{VBF}}, q_1^{2,\text{VBF}}, q_2^{2,\text{VBF}}\}$ for the VBF process or $\mathbf{\Omega}^{\text{assoc}} = \{\theta_1^{\text{VH}}, \theta_2^{\text{VH}}, \theta^{*\text{VH}}, \Phi^{\text{VH}}, \Phi_1^{\text{VH}}, q_1^{2,\text{VH}}, q_2^{2,\text{VH}}\}$ for the VH process (see Fig. 1 and Ref. [26]). It is a challenging task to perform an optimal analysis in a multidimensional space of observables. The MELA method introduced earlier [2, 24–27] is designed to reduce the number of observables to the minimum, while retaining all essential information. Two types of discriminants are defined for the production process. One type of discriminant separates the process with anomalous couplings (denoted as generic BSM here):

$$\mathcal{D}_{\text{BSM}} = \frac{\mathcal{P}_{\text{SM}}(\vec{\Omega})}{\mathcal{P}_{\text{SM}}(\vec{\Omega}) + \mathcal{P}_{\text{BSM}}(\vec{\Omega})}, \tag{11}$$

where this discriminant is called $\mathcal{D}_{0-}$, $\mathcal{D}_{0\text{h}+}$, $\mathcal{D}_{\Lambda 1}$, or $\mathcal{D}_{\Lambda 1}^{\text{Z}\gamma}$, depending on the targeted anomalous coupling. The second type of discriminant isolates the interference contribution:

$$\mathcal{D}_{\text{int}} = \frac{\mathcal{P}^{\text{int}}_{\text{SM}-\text{BSM}}(\vec{\Omega})}{\mathcal{P}_{\text{SM}}(\vec{\Omega}) + \mathcal{P}_{\text{BSM}}(\vec{\Omega})}, \tag{12}$$

where this discriminant is called $\mathcal{D}_{\text{CP}}^{\text{VBF}}$ in the CP-odd amplitude analysis. In the above, $\mathcal{P}$ is the probability for the process (either SM or anomalous signal), and $\mathcal{P}^{\text{int}}_{\text{SM}-\text{BSM}}$ is the interference part of the probability distribution for the process with the mixture of the SM and anomalous contributions. Probabilities are normalized for the matrix elements to give the same cross sections in the relevant phase space of each process. Such normalization leads to a balanced distribution of events in the range between 0 and 1, or between -1 and 1, for the $\mathcal{D}_{\text{BSM}}$ and $\mathcal{D}_{\text{int}}$ discriminants respectively.

The two other observables in Eqs. (11) and (12) rely only on signal matrix elements and are well-defined. One can apply the Neyman-Pearson lemma to prove that, in the absence of detector smearing, they become the minimal and complete set of optimal observables [26, 27] for the measurement of the f_{ai} parameters defined in Section 2.

In application to the CP measurement with the f_{a3} parameter, the two optimal observables are called $\mathcal{D}_{0-}$ and $\mathcal{D}_{\text{CP}}^{\text{VBF}}$, because $J^P = 0^-$ is the BSM hypothesis in this case, and the interference discriminant is an unambiguously CP-sensitive observable. A distinct forward-backward asymmetry in the $\mathcal{D}_{\text{CP}}^{\text{VBF}}$ distribution (forward defined as $\mathcal{D}_{\text{CP}}^{\text{VBF}} > 0$ and backward as $\mathcal{D}_{\text{CP}}^{\text{VBF}} < 0$) appears only in the presence of CP violation. These observables could be defined for both VBF and VH processes. However, since the analysis selection is optimized for the VBF process, the probabilities in the discriminant calculation are defined for the VBF process: $\mathcal{P}_{\text{SM}}(\vec{\Omega})$ and $\mathcal{P}_{\text{BSM}}(\vec{\Omega})$.

3.2 Correlation of two jets in the production of H via gluon fusion

Kinematic distributions of associated particles in gluon fusion production are also sensitive to the quantum numbers and anomalous Hgg couplings. The set of observables in this topology is identical to the VBF process $\mathbf{\Omega}^{\text{assoc}} = \{\theta_1^{\text{ggH}}, \theta_2^{\text{ggH}}, \theta^{*\text{ggH}}, \Phi^{\text{ggH}}, \Phi_1^{\text{ggH}}, q_1^{2,\text{ggH}}, q_2^{2,\text{ggH}}\}$ (see Fig. 1 and Ref. [26]).

Similar to the VBF and VH study, we form optimal $\mathcal{D}_{0-}^{\text{ggH}}$ and $\mathcal{D}_{\text{CP}}^{\text{ggH}}$ observables that are sensitive to CP violation. However, unlike in the VBF production study, the sensitivity to CP

violation using MELA observables in ggH production is comparable to the signed azimuthal difference between two leading jets $\Delta\phi_{jj}$ [47]. Thus, in this study we cross check the results obtained using the MELA discriminants with a simplified approach that does not rely on multivariate techniques and utilizes $\Delta\phi_{jj}$ as the *CP*-sensitive observable. We will refer to these approaches as the "MELA method" and "$\Delta\phi_{jj}$ method" respectively.

4 CMS detector

The main feature of the CMS detector is a superconducting solenoid of 6 m internal diameter, that provides a magnetic field of 3.8 T. Within the volume of the solenoid, there are a silicon pixel and strip tracker detectors, as well as a lead tungstate crystal electromagnetic calorimeter (ECAL) and a brass and scintillator hadron calorimeter (HCAL). Both ECAL and HCAL detectors are composed of a barrel and two endcap sections. Forward calorimeters extend the coverage in pseudorapidity, η. The CMS muon system is comprised of gas-ionization chambers embedded in the steel flux-return yoke outside the CMS solenoid.

The CMS data acquisition system employs a two-tiered trigger system [48] to select events of interest. The first level (L1), composed of custom hardware processors, utilizes information from muon detectors and both calorimeters to select collision events at a rate of about 100 kHz with a latency below 4 μs. The second level (L2) also known as the high-level trigger, further reduces the event acceptance rate to about 1 kHz before data storage by using a full event reconstruction software, optimized for fast processing, running on a computing farm.

A more detailed description of the CMS detector, together with a definition of the coordinate system used and the relevant kinematic variables, can be found in Ref. [49].

4.1 Data and simulation samples

The data samples used in this analysis correspond to integrated luminosities of 36.3 fb^{-1} collected in the 2016, 41.5 fb^{-1} collected in the 2017, and 59.7 fb^{-1} collected in the 2018, for a total of 138 fb^{-1} collected during Run 2 of the LHC at a pp center-of-mass collision energy of 13 TeV [50–52].

MC simulation is used to model signal and background processes in proton-proton (pp) interactions at the LHC and their reconstruction in the CMS detector. All MC samples are interfaced to the PYTHIA [53] generator for parton showering, using version 8.212 for 2016 and 8.230 for 2017 and 2018 data periods. The PYTHIA parameters affecting the description of the underlying event are set to the CUETP8M1 tune [54] for 2016 simulations, and the CP5 tune [55] for 2017 and 2018 simulations. We use NNPDF 3.0 [56] (for 2016 simulation) or 3.1 [57] (for 2017 and 2018) parton distribution functions (PDFs).

Simulated events include the contribution from additional pp interactions within the same or adjacent bunch crossings (pileup) and are weighted to reproduce the observed pileup distribution in data. All the MC samples are further processed through a dedicated CMS detector simulation based on the GEANT4 program [58].

Following the formalism discussed in the previous section, the samples with the SM and anomalous H couplings in VBF and VH production are generated with the JHUGEN [24–27] program at leading-order (LO) in perturbative chromodynamics (QCD). All the simulated scenarios are reweighted to model any other set of H couplings using the MELA [24–27] package that contains a library of matrix elements from JHUGEN for the signal. The VBF and VH JHUGEN SM simulations, after parton showering modeling, are explicitly compared with the NLO QCD SM

simulations produced by POWHEG 2.0 [59–64] and no significant differences are found in kinematic observables. Therefore, the JHUGEN simulation is used to describe kinematics of the VBF and VH processes with anomalous coupling effects in VBF and VH processes, with the expected yields scaled to match the SM theoretical predictions [39] for inclusive cross sections and POWHEG 2.0 prediction of event yields in the categorization of events based on associated particles.

Anomalous ggH events are produced with up to two jets at NLO QCD accuracy using MADGRAPH5_aMC@NLO 2.6.0 [65–67] and are also studied with JHUGEN at LO. The p_{T} and jet multiplicity distributions are then reweighted to match the POWHEG NNLOPS predictions [68, 69]. The relationship between the Hff and Hgg couplings follows JHUGEN with the relative sign of CP-odd and CP-even coefficients opposite to that assumed in MADGRAPH5_aMC@NLO 2.6.0. This choice corresponds to the convention $\epsilon_{0123} = +1$ [38]. The sign convention of the photon field in JHUGEN is opposite to that in MADGRAPH5_aMC@NLO, which leads to the opposite sign of the HZγ couplings. This sign convention depends on the sign in front of the gauge fields in the covariant derivative and this analysis follows $D_\mu = \partial_\mu - \mathrm{i}\frac{e}{2s_w}\sigma^i W^i_\mu + \mathrm{i}\frac{e}{2c_w}B_\mu$ used in JHUGEN [40].

The PYTHIA event generator is used to model the H decay to τ leptons and the decays of the τ leptons. Both scalar and pseudoscalar $\mathrm{H} \to \tau\tau$ decays and their interference have been modeled to confirm that the observables used in the analysis are not sensitive to anomalous H decays. Thus, the default samples are generated with the SM $\mathrm{H} \to \tau\tau$ decay process.

The MADGRAPH5_aMC@NLO [65] generator is used to produce W + jets and $\mathrm{Z} \to \mathrm{ee}/\mu\mu$ + jets samples at LO accuracy with the MLM jet matching and merging [70]. The MADGRAPH5_aMC@NLO generator is also used for diboson production simulated at NLO with the FxFx jet matching and merging [66], whereas POWHEG version 2.0 is used for $\mathrm{t\bar{t}}$ [71] and single top quark (t-channel) production [72], and POWHEG version 1.0 is used for single top quark production associated with a W boson [73].

5 Event selection

The reconstruction of observed and simulated events relies on the particle-flow (PF) algorithm [74], which combines the information from the CMS subdetectors to identify and reconstruct particles emerging from pp collisions. Combinations of these PF candidates are used to reconstruct higher-level objects such as jets, τ candidates, or missing transverse momentum, $\vec{p}_{\mathrm{T}}^{\,\mathrm{miss}}$. The reconstructed vertex with the largest value of summed physics object p_{T}^2 is taken to be the primary pp interaction vertex, where p_{T} is the transverse momentum. The physics objects are the objects constructed by a jet finding algorithm [75, 76] applied to all charged tracks associated with the vertex and the corresponding associated missing transverse momentum.

Electrons are identified with a multivariate discriminant combining several quantities describing the track quality, the shape of the energy deposits in the ECAL, and the compatibility of the measurements from the tracker and the ECAL [77]. Muons are identified with requirements on the quality of the track reconstruction and on the number of measurements in the tracker and the muon systems [78]. A relative isolation variable, I^ℓ, is defined as the total energy deposited in a cone of size of $R < 0.3$ ($R < 0.4$) centered on the electron (muon) direction divided by the p_{T} of the lepton. The expected contribution to the energy sum from pileup interactions is estimated and subtracted from the total. To reject non-prompt or misidentified leptons, we require that $I^\ell < 0.15$.

Jets are reconstructed with an anti-k_T clustering algorithm [79], as implemented in the FASTJET package [76]. The algorithm is based on the clustering of neutral and charged PF candidates within a distance parameter of 0.4. Charged PF candidates not associated with the primary vertex of the interaction are not considered when building jets. An offset correction is applied to jet energies to take into account the contribution from additional pp interactions within the same or nearby bunch crossings. In this analysis, jets are required to have $p_T > 30\,\text{GeV}$ and absolute pseudorapidity $|\eta| < 4.7$, and to be separated from the selected leptons by a distance parameter $\Delta R = \sqrt{(\Delta\eta)^2 + (\Delta\phi)^2}$ of at least 0.5, where ϕ is the azimuthal angle in radians. Data collected in the ECAL endcaps were affected by large amounts of noise during the 2017 run, which led to disagreements between simulation and data. To mitigate this effect, jets used in the analysis of the 2017 data are discarded if they have $p_T < 50\,\text{GeV}$ and $2.65 < |\eta| < 3.139$. Hadronic jets that contain b quarks ("b jets") are identified using a deep neural network, called the DeepCSV algorithm [80].

Hadronically decaying τ leptons, denoted as τ_h, are reconstructed with the hadron-plus-strips algorithm [81, 82], which is seeded with anti-k_T jets with $p_T > 14\,\text{GeV}$. This algorithm reconstructs τ_h candidates based on the number of tracks and the number of ECAL strips with energy deposits within the associated η-ϕ plane and reconstructs one-prong, one-prong+π^0(s), and three-prong decay modes. For this analysis, a deep neural network (DNN) discriminator is used to identify hadronic decays of tau leptons [83]. The input variables to the DNN include variables related to the τ_h isolation, τ_h lifetime, and other detector-related variables. These variables serve as input to a DNN, which provides an output discriminant. The threshold on the output discriminant depends on the τ_h p_T and provides a τ_h ID and reconstruction efficiency of about 60%. Two other DNNs are used to reject electrons and muons misidentified as τ_h candidates using dedicated criteria based on the consistency between the measurements in the tracker, the calorimeters, and the muon detectors.

The missing transverse momentum $\vec{p}_T^{\,\text{miss}}$ is defined as the negative vector sum of the transverse momenta of all PF candidates [84].

The invariant mass of the $\tau\tau$ system $m_{\tau\tau}$ is a key variable for separating H candidate events from the background in this analysis. The $m_{\tau\tau}$ is reconstructed using the FASTMTT algorithm, which is similar to the SVFIT algorithm [85] used in previous CMS publications except that it uses a simplified mass likelihood function to reduce the computation time. This algorithm makes use of the $\vec{p}_T^{\,\text{miss}}$ and its uncertainty with the four-vectors of both reconstructed τ lepton candidates to calculate a more accurate estimate of the mass of the parent boson and the full four-momenta of the H decay products needed to calculate MELA kinematic observables discussed in Sec. 3.

5.1 Event categorization

Selected events are classified according to four decay channels, $e\mu$, $e\tau_h$, $\mu\tau_h$, and $\tau_h\tau_h$. The resulting event samples are made mutually exclusive by discarding events that have additional loosely identified and isolated electrons or muons.

The largest irreducible source of background is Drell-Yan production of $Z \to \tau\tau$, while the dominant background sources with jets misidentified as leptons are QCD multijet and W + jets. Other contributing background sources are $t\bar{t}$, single top, $Z \to ee$, $Z \to \mu\mu$, and diboson production.

The two tau leptons assigned to the H decay are required to have opposite charges. The trigger requirements, geometrical acceptances, and transverse momentum criteria are summarized in

Table 2. The p_T thresholds in the lepton selections are optimized to increase the sensitivity to the $H \to \tau\tau$ signal, while also satisfying the trigger requirements. The pseudorapidity selections are driven by reconstruction and trigger requirements.

Table 2: Kinematic selection requirements for the four di-τ decay channels. The trigger requirement is defined by a combination of trigger candidates with p_T over a given threshold, indicated inside parentheses in GeV. The pseudorapidity thresholds come from trigger and object reconstruction constraints. The p_T thresholds for the lepton selection are driven by the trigger requirements, except for the τ_h candidate in the $\mu\tau_h$ and $e\tau_h$ channels, and the sub-leading lepton in the $e\mu$ channel, where they have been optimized to increase the analysis sensitivity.

Channel	Trigger requirement	Year	Minimal lepton selection		
			p_T (GeV)	η	Isolation
$\tau_h\tau_h$	$\tau_h(35)$ & $\tau_h(35)$	2016	$p_T^{\tau_h} > 40$	$\lvert\eta^{\tau_h}\rvert < 2.1$	DNN τ_h ID
	$\tau_h(40)$ & $\tau_h(40)$	2017, 2018			
$\mu\tau_h$	$\mu(22)$	2016	$p_T^{\mu} > p_T^{trigger} + 1\,\text{GeV}$	$\lvert\eta^{\mu}\rvert < 2.1$	$I^{\mu} < 0.15$
	$\mu(19)$ & $\tau_h(21)$	2016	$p_T^{\tau_h} > 30$	$\lvert\eta^{\tau_h}\rvert < 2.3$	DNN τ_h ID
	$\mu(24)$	2017, 2018			
	$\mu(20)$ & $\tau_h(27)$	2017, 2018			
$e\tau_h$	$e(25)$	2016	$p_T^{e} > p_T^{trigger} + 1\,\text{GeV}$	$\lvert\eta^{e}\rvert < 2.1$	$I^{e} < 0.15$
	$e(27)$	2017	$p_T^{\tau_h} > 30$	$\lvert\eta^{\tau_h}\rvert < 2.3$	DNN τ_h ID
	$e(32)$	2018			
	$e(24)$ & $\tau_h(30)$	2017, 2018			
$e\mu$	$e(12)$ & $\mu(23)$	all years	$p_T^{e} > 15$, $p_T^{\mu} > 24$	$\lvert\eta^{e}\rvert < 2.4$	$I^{e} < 0.15$
	$e(23)$ & $\mu(8)$	all years	$p_T^{\mu} > 15$, $p_T^{e} > 24$	$\lvert\eta^{\mu}\rvert < 2.4$	$I^{\mu} < 0.15$

In the $\ell\tau_h$ channels, the large W + jets background is reduced by requiring the transverse mass, m_T, to be less than 50 GeV. The transverse mass is defined as follows,

$$m_T \equiv \sqrt{2 p_T^{\ell} p_T^{miss} [1 - \cos(\Delta\phi)]}, \tag{13}$$

where p_T^{ℓ} is the transverse momentum of the electron or muon and $\Delta\phi$ is the azimuthal angle between the lepton direction and the $\vec{p}_T^{miss}$ direction.

In the $e\mu$ and $\ell\tau_h$ channels, events with b jets are vetoed to reduce the background from $t\bar{t}$ production. In the $e\mu$ channel, this background is further mitigated by requiring $p_\zeta = p_\zeta^{miss} - 0.85\, p_\zeta^{vis} > -35\,\text{GeV}$, where p_ζ^{miss} is the component of $\vec{p}_T^{miss}$ along the bisector of the transverse momenta of the two leptons and p_ζ^{vis} is the sum of the components of the lepton transverse momenta along the same direction [86].

Event categories are designed to increase the sensitivity to the signal by isolating regions with large signal-to-background ratios, and to provide sensitivity to the Hgg and HVV parameters. They follow closely the selection in Ref. [87]:

- 0-jet category: This category targets H events produced via gluon fusion. Events containing no jets with $p_T > 30\,\text{GeV}$ are selected.
- VBF category: This category targets H events produced via the VBF process. Events are selected with at least two jets with $p_T > 30\,\text{GeV}$. In the $e\mu$ and $\ell\tau_h$ channels the invariant mass of the two leading jets m_{jj} is required be larger than 300 GeV. In the $\tau_h\tau_h$ channel we require the separation between the two leading jets in pseudorapidity $|\Delta\eta_{jj}|$ to be greater than 2.5, and the transverse component of the vector sum

of the $\vec{p}_{\mathrm{T}}^{\,\mathrm{miss}}$ and the $\vec{p}_{\mathrm{T}}$ of the visible decay products of the tau leptons, defined as $\vec{p}_{\mathrm{T}}^{\,\tau\tau}$, to have a magnitude ($p_{\mathrm{T}}^{\tau\tau}$) greater than 100 GeV.

- Boosted category: This category contains all the events that do not enter one of the previous categories, namely events with one jet and events with several jets that fail the requirements of the VBF category. It targets events with a H produced in gluon fusion and recoiling against an initial state radiation jet.

6 Background estimation

In this section we describe the background processes to the $\mathrm{H} \to \tau\tau$ signal and methods to estimate their contributions. The major background is from Drell-Yan production where the Z boson decays to a pair of tau leptons, followed by backgrounds from jets misidentified as tau lepton candidates. Whenever possible we rely on data to estimate background contributions. The data, signal, and background predictions in the VBF category, which is most sensitive to anomalous effects in production are illustrated in Fig. 2.

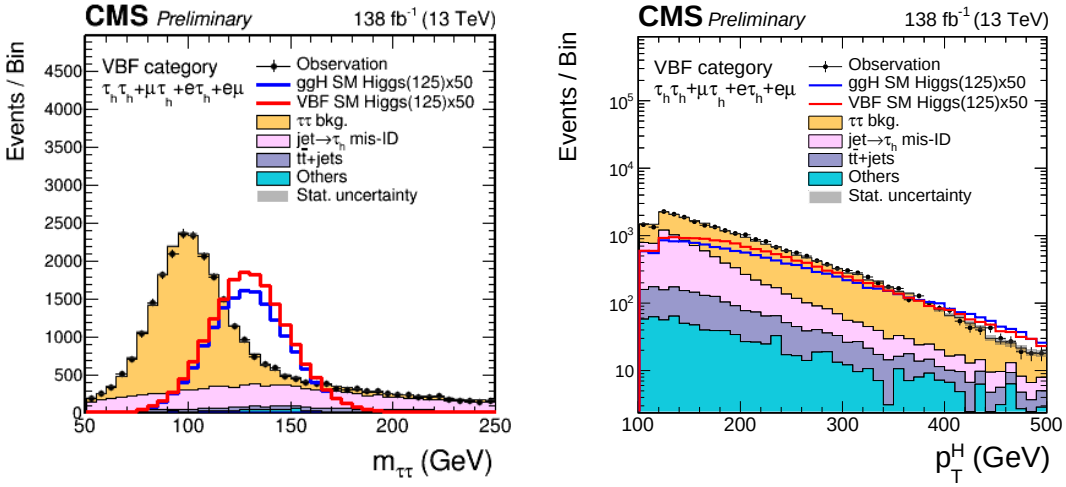

Figure 2: Di-tau lepton candidate mass distribution (left) and p_{T} spectrum of the selected H candidates (right) in the VBF category. All events selected in the eμ, eτ_{h}, $\mu\tau_{\mathrm{h}}$, and $\tau_{\mathrm{h}}\tau_{\mathrm{h}}$ final states are included. Only statistical uncertainties are shown.

6.1 Backgrounds due to $\tau\tau$ events

The Drell-Yan $\mathrm{Z}/\gamma^* \to \tau\tau$ process is the dominant background to the $\mathrm{H} \to \tau\tau$ signal as both processes share the same final state and have very similar kinematic properties. Additionally, several other process such as $\mathrm{t\bar{t}}$ can produce a $\tau\tau$ final state. Given the dominance of these backgrounds in data, we rely on an embedding method [88] to simulate them: i) in a dedicated control region, $\mathrm{Z}/\gamma^* \to \mu\mu$ candidate events are selected from data; ii) calorimeter deposits and tracks produced by the pair of muons in the event are removed; iii) the muons in the event are replaced with simulated tau leptons with identical four-vectors; and iv) the PYTHIA generator is used to model the decay of the τ leptons in the same way as a typical $\mathrm{Z}/\gamma^* \to \tau\tau$ decay. The embedding process is performed separately for each decay channel and results in greatly improved statistical accuracy compared to that of a typical MC simulation. Using data to describe effects such as pileup and detector noise results in a much more reliable description

of $p_{\mathrm{T}}^{\mathrm{miss}}$ and jet related variables, which in turn reduces systematic uncertainties arising from, for example, jet energy corrections.

6.2 Background due to jet misidentification

One of the major backgrounds to the $\mathrm{H} \to \tau\tau$ signal in the $\mathrm{e}\tau_{\mathrm{h}}$, $\mu\tau_{\mathrm{h}}$, and $\tau_{\mathrm{h}}\tau_{\mathrm{h}}$ channels originates from events where a jet is misidentified as a hadronically decaying tau lepton τ_{h}. We refer to such backgrounds as jet $\to \tau_{\mathrm{h}}$ processes. The background processes include multijet (QCD) production, W+jets, $\mathrm{t\bar{t}}$, and diboson processes. As the jet$\to \tau_{\mathrm{h}}$ misidentification rates are typically $\sim$ 0.1–1%, the use of MC simulation to model this background is undesirable due to the statistical limitation and systematic uncertainty associated with the correct modeling of the detector response to jets identified as tau leptons. Thus, we rely on data to model this background, using the so-called "fake factor" method [89].

To estimate the jet $\to \tau_{\mathrm{h}}$ contamination in the signal region we select τ_{h} candidates that fulfill all event selection criteria with the exception of containing τ_{h} candidates that fail the nominal identification requirements but pass a looser requirement on the DNN. This selection is referred to in the following as "relaxed". In the $\tau_{\mathrm{h}}\tau_{\mathrm{h}}$ channel either or both τ_{h} may originate from a jet $\to \tau_{\mathrm{h}}$ but the dominant process is multijet QCD, which results in two jet $\to \tau_{\mathrm{h}}$ candidates. In this case we require only that the leading τ_{h} fail the nominal identification. These selected events are then scaled on an event-by-event basis by the fake factors, which are ratios between the nominal and relaxed τ_{h} identification rates.

The fake factors are determined separately for each channel, and for each of the dominant processes contributing to the jet $\to \tau_{\mathrm{h}}$ background. For the $\tau_{\mathrm{h}}\tau_{\mathrm{h}}$ channel, the jet $\to \tau_{\mathrm{h}}$ background originates almost entirely from QCD multijet events, and therefore fake factors are derived only for this process. For the $\mathrm{e}\tau_{\mathrm{h}}$ and $\mu\tau_{\mathrm{h}}$ channels, separate fake factors are derived for QCD multijet, W+jets, and $\mathrm{t\bar{t}}$ processes. The QCD and W+jet fake factors are measured in dedicated control regions enriched with the events from the given process. The QCD control region is defined by inverting the opposite-sign charge requirement on the di-τ candidate pair. The W+jet control region is defined by selecting events with $m_{\mathrm{T}} > 70\,\mathrm{GeV}$. Obtaining a $\mathrm{t\bar{t}}$ control region with high purity is not possible, and the fake factors are therefore measured in simulation for this sub-dominant process. We parameterize the fake factors as a function of the tau lepton p_{T}. As events in this study are categorized primarily by the number of jets in the event, the fake factors are measured in jet multiplicity bins: no jets, one jet, and two or more jets.

The fake factors for each of the individual processes are then weighted into an overall fake factor to account for their contributions in the signal region. For the $\mathrm{e}\tau_{\mathrm{h}}$ and $\mu\tau_{\mathrm{h}}$ channels, the fake factors measured for the W+jets process are weighted to also account for all other sub-dominant jet $\to \tau_{\mathrm{h}}$ processes (all processes except multijet QCD, W+jets, and $\mathrm{t\bar{t}}$). For the $\tau_{\mathrm{h}}\tau_{\mathrm{h}}$ channel, the multijet QCD fake-factors account also for all other sub-dominant processes where the leading τ_{h} is a misidentified jet. The events in which the sub-leading τ_{h} is a misidentified jet and the leading τ_{h} candidate is a genuine τ lepton are modeled via simulation; these events constitute only a small fraction ($\mathcal{O}(2\%)$) of the total misidentified jet background in this channel.

Finally, the fake factors are further corrected to accommodate residual differences observed when applying the measured fake-factors to events in control regions. Such corrections are needed to account for: differences in the jet $\to \tau_{\mathrm{h}}$ misidentification rates in control and signal regions arising from, for example, slight differences in the jet flavor compositions; the choices of functional forms for parameterizing the p_{T} dependence; the finite binning of the parameterizing variables; and the omission of dependencies on kinematic or topological variables.

In the eμ channel, one of the minor backgrounds stems from the multijet QCD process, where at least one jet is misidentified as an electron or a muon candidate. The majority of these events involve $b\bar{b}$ production, with electron and muon candidates produced in semi-leptonic decays of heavy-flavor quarks. This background is estimated from a sideband region using events with an electron and a muon with same-sign (SS) electric charges. Scale factors are then applied to extrapolate from this sideband region to the signal region. These so-called OS/SS scale factors are derived from a control region where the muons pass a relaxed isolation requirement but fail the signal region isolation criteria. The dependence of the OS/SS factors on the ΔR between the two leptons and jet multiplicity in the event is taken into account. A correction is also applied to account for any bias introduced by the inversion of the isolation requirement on the muon candidate. Finally, we subtract contributions from known SM processes using embedded and MC simulation samples.

6.3 Other backgrounds processes

The remaining backgrounds include Drell-Yan processes, where the Z boson decays to a pair of electrons or muons and one or more of the final state leptons is misidentified as the tau lepton, as well as $t\bar{t}$, single top quark and multiboson production with fewer than two genuine τ leptons and additional electrons or muons that are misidentified as leptonically or hadronically decaying tau leptons. These backgrounds are small and we rely on MC simulation to estimate their contribution to the signal region. To avoid double-counting of backgrounds arising from jet misidentification, we remove the events with the generator-level quark or gluon matched to the reconstructed tau lepton candidate in the final state. Similarly, Drell-Yan MC events as well as any other MC simulation events with two genuine τ leptons are discarded to avoid overlap with the embedded samples.

6.4 Corrections to simulated data

To improve the agreement between the signal and background processes modeled with simulations and the data, the following corrections are applied to the simulated events (including $\tau\tau$-embedded events for corrections pertaining to the simulated tau leptons):

- The pileup distribution in simulation is reweighted in order to match the pileup in data.
- Muon and electron channels are corrected to account for their trigger efficiencies, reconstruction, identification, and isolation requirements. The channels containing τ_h are corrected for their trigger efficiencies, reconstruction, and identification requirements. Corrections are also applied to events including $e \to \tau_h$ and $\mu \to \tau_h$ candidates to account for differences in the misidentification probabilities.
- For the eμ and $\ell\tau_h$ channels, corrections are applied to account for differences in the number of events passing the b jet veto as a result of variations in the probabilities for jets to be tagged as b jets.
- The τ_h energy scales are corrected per decay mode to match the energy scale in data. Separate corrections are derived for τ_h candidates that originate from genuine hadronically decaying tau leptons and those that originate from electron and muon misidentifications. The electron energy scale is adjusted in data and simulation using the Z mass peak, and the resolution of the simulated electrons is also adjusted to match the data.
- Jet energy scale corrections are applied to both data and simulated events, and the energy resolution of simulated jets is adjusted to match the resolution in data. For

the Drell-Yan, W+jets, and H events estimated from simulation, recoil corrections are applied to the p_T^{miss} based on the vector difference of the measured p_T^{miss} and the total transverse momentum of the neutrinos from the Z, W, or H decay products.

- The Z mass and p_T distributions are reweighted to better match the distributions in data. These corrections are derived by comparing simulated $Z \to \mu\mu$ events to the equivalent events selected in data. The size of the corrections are typically less than 20%. For $t\bar{t}$ events, the top p_T spectra are also reweighted to match the p_T spectra in data. The procedure used to derive these corrections is described in Ref. [90]. The size of the corrections are less than 20%.

7 Systematic uncertainties

A variety of systematic uncertainties are taken into account in the analysis. The uncertainty model consists of normalization uncertainties that only scale the yield of a distribution while leaving its shape unchanged, and shape uncertainties that also alter the shapes of the distributions. The leading systematic uncertainty sources result from the jet energy scales and resolutions, and the limited statistics of the simulated events. All systematic uncertainties are implemented in the form of nuisance parameters in the likelihood, which can be further constrained by the fit to the data. The uncertainties considered in this analysis are summarized in Table 3 and detailed below.

The integrated luminosities of the 2016, 2017, and 2018 data-taking periods are individually known with uncertainties in the 1.2–2.5% range [50–52], while the total Run 2 (2016–2018) integrated luminosity has an uncertainty of 1.6%, the improvement in precision reflecting the (uncorrelated) time evolution of some systematic effects.

The uncertainties in the muon (electron) reconstruction, identification, and isolation amount to 1% (2%). The electron and muon triggers contribute an additional 2% uncertainty in the yield of simulated processes. The uncertainty in the electron energy scale depends on p_T and η and is typically less than 1%. The muon energy scale uncertainty varies between 0.4 and 2.7% depending on η.

The τ_h reconstruction and identification efficiency is measured in three p_T bins (30-35, 35-40, 40+ GeV) or four τ_h decay mode bins and is statistically dominated. The uncertainty is taken to be uncorrelated for the individual measurements and ranges between 2–3%. In addition, a yield uncertainty of 3% is taken into account for real τ_h candidates due to the discrimination against electrons and muons. An additional uncertainty is applied for the τ_h reconstruction in the embedded samples to account for differences in the charged hadrons and π^0 reconstruction efficiencies. The uncertainty on the τ_h trigger efficiencies depends on the p_T and decay mode of the τ_h candidates, and is therefore treated as a shape uncertainty. For electrons and muons misidentified as τ_h candidates, an uncertainty derived in bins of p_T, η, and decay mode of the misidentified τ_h candidate is applied and amounts to between 9–40% and 10–70%, respectively. The uncertainty in the τ_h energy scale ranges between 0.2–1.1% depending on the decay mode. For electrons and muons misidentified as τ_h candidates, the uncertainty in the energy scale amounts to 1% for muons and between 1–6.5% for electrons.

During the 2016 and 2017 data taking, a gradual shift in the timing of the inputs of the ECAL L1 trigger in the forward endcap region ($2.5 < |\eta| < 3.0$) led to a specific inefficiency. It affects predominantly events with high p_T electrons and jets. For events containing an electron (jet) with p_T larger than $\approx$ 50 GeV ($\approx$ 100 GeV), in the region of $2.5 < |\eta| < 3.0$ the efficiency loss is 10–20%, depending on p_T, η, and the data taking period. Additional correction factors are

Table 3: Sources of systematic uncertainties.

Uncertainty	Magnitude
τ_h ID	p_T/decay-mode dependent (2–3%)
τ_h separation from e/μ	3%
e $\to \tau_h$ ID	η dependent (9–40%)
$\mu \to \tau_h$ ID	η dependent (10–70)%
e ID	2%
μ ID	1%
b jet veto	0–10%
Luminosity	1.6%
Trigger	2% for e/μ, p_T/decay-mode dep. for τ_h ($\mathcal{O}$(10%))
$t\bar{t}$ cross section	4.2%
Diboson cross section	5%
Single top cross section	5%
Drell-Yan cross section	2%
L1 trigger timing (2016 and 2017)	Event-dependent (0.2–15%)
$\mathcal{B}(H \to \tau\tau)$	2.1%
τ_h energy scale	Decay-mode dependent (0.2–1.2%)
e $\to \tau_h$ energy scale	Decay-mode dependent (1–7%)
$\mu \to \tau_h$ energy scale	1%
Electron energy scale	p_T/η dependent (< 1.25%)
Muon energy scale	η dependent 0.4–2.7%
Jet energy scale	p_T/η dependent ($\sim$ 0.5–14%)
Jet energy resolution	η dependent (2–95%)
p_T^{miss} unclustered energy scale	Event-dependent ($\sim$ 0–20%)
p_T^{miss} recoil corrections	0.3–5.8%
Jet $\to \tau_h$ mis-ID	Event-dependent ($\mathcal{O}$(10%))
QCD multijet in the eμ channel	Event-dependent ($\mathcal{O}$(20%))
Embedded yield	4%
$t\bar{t}$ in embedded	10%
Signal theoretical uncertainty	Event-dependent (up to $\sim$ 25%)
Top p_T reweighting	p_T dependent (0–21%)
DY p_T-mass reweighting	p_T/mass dependent (0–11%)

applied to the simulation to account for this inefficiency. This results in a small decrease in the estimated signal and background yields, for example, the inclusive SM VBF yields are reduced by about 2–3%. The uncertainty on these correction factors ranges between 0.2 and 15%.

Uncertainties in the jet energy scale come from different sources and with partial correlations. These sources typically affect different regions of the detector and their magnitude depends on the jet kinematics. Uncertainties in the jet energy resolution are also taken into account. These uncertainties create migrations between categories defined on the basis of the jet multiplicity or m_{jj}, and affect the shapes of the $\Delta\phi_{jj}$ and MELA discriminants. For all MC samples without recoil corrections applied, the uncertainties in the jet energy scale and resolution are propagated to the $\vec{p}_{\mathrm{T}}^{\,\mathrm{miss}}$.

For simulated events that have recoil corrections, the uncertainties in the resolution and response of the $\vec{p}_{\mathrm{T}}^{\,\mathrm{miss}}$ are derived as part of the estimate of the recoil corrections. Other processes suffer from uncertainties in the energy measurement for the energy depositions in the calorimeter, not associated with jets and photon candidates, so-called unclustered energy scale uncertainties. The magnitudes of these uncertainties depend on the p_{T}, η, and types of the unclustered PF candidates.

The yield uncertainty related to discarding events with a b-tagged jet varies up to 10% for background with heavy-flavor jets. The uncertainty in the mis-tagging rate of gluon and light-flavor jets is less than 1%.

For background with jet $\to \tau_{\mathrm{h}}$ misidentifications, the uncertainties on the measured fake factors are propagated to the background predictions as shape uncertainties. This includes statistical uncertainties on the fitted functions as well as systematic uncertainties coming from residual differences observed in control regions. Similarly, for the multijet QCD estimation in the $\mathrm{e}\mu$ channel uncertainties in the OS/SS extrapolation factors are taken into account.

Uncertainties related to the embedding method are taken into account in addition to those pertaining to the simulated τ decay products described previously. Embedded samples include all events with two τ candidates, essentially Drell-Yan events, but also contain small fractions of diboson and $\mathrm{t\bar{t}}$ events. A shape uncertainty is applied to take into account the contamination from these non Drell-Yan events, which amounts to 10% of the $\mathrm{t\bar{t}}$ and diboson contribution to embedded samples, as estimated from simulation. Data events with muons are selected with a muon trigger before embedding the simulated τ leptons. The uncertainty in this trigger requirement amounts to 4%.

Uncertainties in the $\mathrm{t\bar{t}}+$jets, Drell-Yan, diboson, and single top quark production cross sections amount to 4.2, 2.0, 5.0, and 5.0%, respectively. This includes uncertainties due to missing higher order corrections, the PDF, and the running coupling α_{S}. For the $\mathrm{t\bar{t}}+$jets cross section the uncertainty on the top quark mass is also included. The top p_{T} and Drell-Yan p_{T} and mass spectra are reweighted. For the top samples the size of the correction is taken as the uncertainty, while for the Drell-Yan the correction is varied by 10%.

The theoretical uncertainty in the branching fraction of the H to τ leptons includes a 1.7% uncertainty due to missing higher order corrections, a 1% parametric uncertainty on the quark masses, and a 0.62% parametric uncertainty on α_{S}. The inclusive uncertainty related to the PDFs amounts to 3.2, 2.1, 1.8, and 1.3%, respectively, for the ggF, VBF, WH, and ZH production modes [39]. Acceptance uncertainties for the ggH signal due to renormalization and factorization scale variations are applied following the uncertainty schemes proposed in Ref.[39]. Acceptance uncertainties for the VBF signal due to renormalization and factorization scale variations are applied as yield uncertainties. The sizes of the uncertainties are typically smaller than

5%.

Uncertainties arising from the limited statistics of the simulated events, or data control regions, are taken into account. They are considered for all bins of the distributions used to extract the results.

8 Analysis of ggH production

In this section we first review the analysis methods employed to extract the Hgg anomalous coupling parameters. In Section 8.1 we describe the MELA method from which we obtain our most stringent limits on the anomalous coupling parameters. The $\Delta\phi_{jj}$ method, which is used to cross check the results obtained by the MELA method, is briefly described in Section 8.2. The results obtained are then presented in Section 8.3.

8.1 The MELA method

The multivariate analysis of the Hgg vertex relies on a combination of simple neural networks and MELA discriminants. The former provide optimal separation of the dominant backgrounds for a given channel from the H production, while the latter offer powerful handles to distinguish different signal hypotheses.

A feed-forward network containing two hidden layers is used in each channel. As dominant backgrounds vary by channel, the observables used in the neural network training change and therefore the architecture of the network is modified for each channel. The number of nodes per layer is kept to a minimum to reduce the complexity of the neural network without compromising its performance. As sensitivity to the Hgg anomalous coupling is maximal for events with kinematics similar to those of VBF production, we use VBF signal events as the signal process for all neural networks. This provides the added benefit that the same network can be used in the analysis of both ggH and VBF production processes.

The simplest neural network is employed in the $e\tau_h$ and $\mu\tau_h$ channels where the background is dominated by the $Z \to \tau\tau$ production. Thus, a simple binary classifier is trained to distinguish VBF production from the $Z \to \tau\tau$ process. We use all seven MELA input variables, $m_{\tau\tau}$, m_{jj}, and $p_T^{\tau\tau}$ as input features for the network.

Multiclass neural networks are utilized in the $\tau_h\tau_h$ and $e\mu$ channels due to the presence of two dominant backgrounds in each channel. In the $\tau_h\tau_h$ channel, a network is trained to sort events in three classes: events that are likely to be from the $Z \to \tau\tau$ production, VBF Higgs production, and background events from processes with jets misidentified as τ_h candidates, using the same features as the $\ell\tau_h$ network. For the $e\mu$ channel, the network is trained to classify events into three classes: $Z \to \tau\tau$, VBF, and $t\bar{t}$. The $e\mu$ channel utilizes the same features as the $\ell\tau_h$ network, but also includes the jet multiplicity and p_ζ.

For the binary classifiers we use the neural network output scores as discriminating variables, whereas for the multiclass networks we use the output scores for the VBF signal classes. We will refer to these discriminants collectively as $\mathcal{D}_{NN}$.

Three MELA discriminants are used in the Hgg analysis, each providing separation between different signal hypotheses. In order to separate ggH production from VBF production, $\mathcal{D}_{2jet}^{VBF}$ as defined in Eq. 14 is used. The discriminant $\mathcal{D}_{0-}^{ggH}$, defined in Eq. 15, is used to separate ggH produced with the SM couplings from ggH produced with a pure pseudoscalar coupling. Lastly, $\mathcal{D}_{CP}^{ggH}$, defined in Eq. 16, provides sensitivity to the interference term in the coupling.

Table 4: List of observables used in the MELA method.

Category	Observable	Goal
0-jet	$m_{\tau\tau}$	Separate H signal from backgrounds
Boosted	$p_{\mathrm{T}}^{\tau\tau}$, $m_{\tau\tau}$	Separate H signal from backgrounds
VBF	$\mathcal{D}_{\mathrm{NN}}$	Separate VBF-like H signal from backgrounds
VBF	$\mathcal{D}_{\mathrm{2jet}}^{\mathrm{VBF}}$	Separate ggH from VBF H production
VBF	$\mathcal{D}_{0-}^{\mathrm{ggH}}$ ($\mathcal{D}_{0-}$)	Separate BSM from SM ggH (HVV)
VBF	$\mathcal{D}_{\mathrm{CP}}^{\mathrm{ggH}}$ ($\mathcal{D}_{\mathrm{CP}}^{\mathrm{VBF}}$)	Sensitive to the interference between the CP-even and CP-odd contributions to the Hgg (HVV) coupling

$$\mathcal{D}_{\mathrm{2jet}}^{\mathrm{VBF}} = \frac{\mathcal{P}_{\mathrm{SM}}^{\mathrm{ggH}} + \mathcal{P}_{0-}^{\mathrm{ggH}}}{\mathcal{P}_{\mathrm{SM}}^{\mathrm{ggH}} + \mathcal{P}_{0-}^{\mathrm{ggH}} + \mathcal{P}_{\mathrm{SM}}^{\mathrm{VBF}}} \tag{14}$$

$$\mathcal{D}_{0-}^{\mathrm{ggH}} = \frac{\mathcal{P}_{\mathrm{SM}}^{\mathrm{ggH}}}{\mathcal{P}_{\mathrm{SM}}^{\mathrm{ggH}} + \mathcal{P}_{0-}^{\mathrm{ggH}}} \tag{15}$$

$$\mathcal{D}_{\mathrm{CP}}^{\mathrm{ggH}} = \frac{\mathcal{P}_{\mathrm{SM}-0-}^{\mathrm{ggH}}}{\mathcal{P}_{\mathrm{SM}}^{\mathrm{ggH}} + \mathcal{P}_{0-}^{\mathrm{ggH}}} \tag{16}$$

The results of the analysis are extracted with a global maximum likelihood fit based on signal-sensitive observables. We summarize the observables utilized in the analysis of the ggH production in Table 4. As the same set of observables is used in the HVV study, except for the superscripts of anomalous-coupling specific MELA discriminators, we define them in Table 4 as well.

We use four observables in total to construct our fitted distributions in the VBF category: $\mathcal{D}_{0-}^{\mathrm{ggH}}$, $\mathcal{D}_{\mathrm{CP}}^{\mathrm{ggH}}$, $\mathcal{D}_{\mathrm{NN}}$, and $\mathcal{D}_{\mathrm{2jet}}^{\mathrm{VBF}}$. The selected events are binned in multidimensional histograms (templates) of these observables. The binning of these templates has been optimized to ensure sufficient statistical populations of all bins, to retain kinematic information, and for memory usage and speed of computer calculations.

The inclusion of the $\mathcal{D}_{\mathrm{CP}}^{\mathrm{ggH}}$ observable is intended to bring sensitivity to the sign of the interference between the CP-even and CP-odd contributions, which would manifest as an asymmetry between the number of events detected with positive and negative values of $\mathcal{D}_{\mathrm{CP}}^{\mathrm{ggH}}$. We therefore include two bins in this discriminant, $\mathcal{D}_{\mathrm{CP}}^{\mathrm{ggH}} < 0$ and $\mathcal{D}_{\mathrm{CP}}^{\mathrm{ggH}} \geq 0$. It should be noted that $\mathcal{D}_{\mathrm{CP}}^{\mathrm{ggH}}$ is symmetric about $\mathcal{D}_{\mathrm{CP}}^{\mathrm{ggH}} = 0$ in the absence of CP-violation, and this symmetry is enforced for the background and CP-conserving signal templates to reduce the influence of statistical fluctuations. For the remaining three observables we allocate more bins to those that have a stronger influence on the expected sensitivity. For the $\ell\tau_{\mathrm{h}}$ channels, we use 10, 8, and 4 equally sized bins for $\mathcal{D}_{0-}^{\mathrm{ggH}}$, $\mathcal{D}_{\mathrm{NN}}$, and $\mathcal{D}_{\mathrm{2jet}}^{\mathrm{VBF}}$, respectively. For the eμ channel, which is the least sensitive channel in this analysis, we respectively use 3, 2, and 4 bins for these observables. In all cases we additionally check for bins where the total statistical uncertainty on the background prediction is in excess of 50%, and merge such bins with their neighbors to prevent cases where bins have very low statistical populations. For the $\tau_{\mathrm{h}}\tau_{\mathrm{h}}$ channel, it was not possible to define a suitable set of equally spaced bins that fulfilled the optimization criteria without

unduly compromising the sensitivity to f_{a3}^{ggH}. Therefore, we employ variable bin widths for the $\mathcal{D}_{0-}^{\mathrm{ggH}}$, $\mathcal{D}_{\mathrm{NN}}$, and $\mathcal{D}_{\mathrm{2jet}}^{\mathrm{VBF}}$ observables; selecting bin boundaries that optimize the expected sensitivity while minimizing the total number of bins in the templates.

We use two observables to construct our templates in the Boosted category, $m_{\tau\tau}$ and $p_{\mathrm{T}}^{\tau\tau}$, and one observable in the 0-jet category, $m_{\tau\tau}$. There are no dedicated observables sensitive to anomalous couplings in these channels, as the events either have fewer than the two jets needed to construct the observables, or do not display significant separation between different signal scenarios to justify their inclusion. These categories are included in the fit nonetheless to constrain backgrounds and to provide sensitivity to the inclusive ggH cross section. The chosen binning in these categories is thus similar to what was employed in previous CMS measurements [87].

Example distributions of the observables in the most sensitive $\tau_{\mathrm{h}}\tau_{\mathrm{h}}$ and $\mu\tau_{\mathrm{h}}$ channels are given in Fig. 3.

8.2 The $\Delta\phi_{jj}$ method

The $\Delta\phi_{jj}$ method is based on the strategy proposed in Ref. [47]. The signed azimuthal separation between the two leading jets $\Delta\phi_{jj}$ provides sensitivity to the CP properties of the Hgg vertex. The sign of $\Delta\phi_{jj}$ is defined by ordering the jets in η:

$$\Delta\phi_{jj} = \phi(j_1) - \phi(j_2), \text{ with } \eta(j_1) < \eta(j_2), \tag{17}$$

which ensures that the observable is sensitive to the interference between the CP-even and CP-odd contributions [29, 30, 91]. The VBF-like ggH events are targeted as they have been shown to be most sensitive to the Hgg anomalous couplings [47].

The event selection and categorization follows closely those described in Section 5.1. The only notable differences are in the definitions of the VBF signal categories, which are therefore described below.

The VBF category definition described in Section 5.1 is adopted for the eμ and $\ell\tau_{\mathrm{h}}$ channels. For the $\tau_{\mathrm{h}}\tau_{\mathrm{h}}$ channel, the VBF category selections defined previously for the $\ell\tau_{\mathrm{h}}$ channels are utilized. The selected VBF-like events are then further subdivided into four categories based on m_{jj} and $p_{\mathrm{T}}^{\tau\tau}$ to enhance the separation between different CP scenarios and to provide additional differentiation between the signal and backgrounds. The four categories are defined as follows:

- Loose-m_{jj} category: this category selects events with $m_{jj} < 500\,\mathrm{GeV}$ and $p_{\mathrm{T}}^{\tau\tau} < 150\,\mathrm{GeV}$.
- Loose-m_{jj} boosted category: this category selects events with $m_{jj} < 500\,\mathrm{GeV}$ and $p_{\mathrm{T}}^{\tau\tau} \geq 150\,\mathrm{GeV}$.
- Tight-m_{jj} category: this category selects events with $m_{jj} \geq 500\,\mathrm{GeV}$ and $p_{\mathrm{T}}^{\tau\tau} < 150\,\mathrm{GeV}$.
- Tight-m_{jj} boosted category: this category selects events with $m_{jj} \geq 500\,\mathrm{GeV}$ and $p_{\mathrm{T}}^{\tau\tau} \geq 150\,\mathrm{GeV}$.

We summarize the observables utilized in Table 5. In this case we use 2D templates in the VBF categories to extract the results. These templates are constructed using the $\Delta\phi_{jj}$ and $m_{\tau\tau}$ observables. We use 12 bins for $\Delta\phi_{jj}$, equally spaced between -3.2 and 3.2. Variable bin widths are used for the $m_{\tau\tau}$ observable, where the bin boundaries are selected to capture the peaking structures of the signal distributions close to $m_{\tau\tau} \sim 125\,\mathrm{GeV}$. The initial choice of the $m_{\tau\tau}$

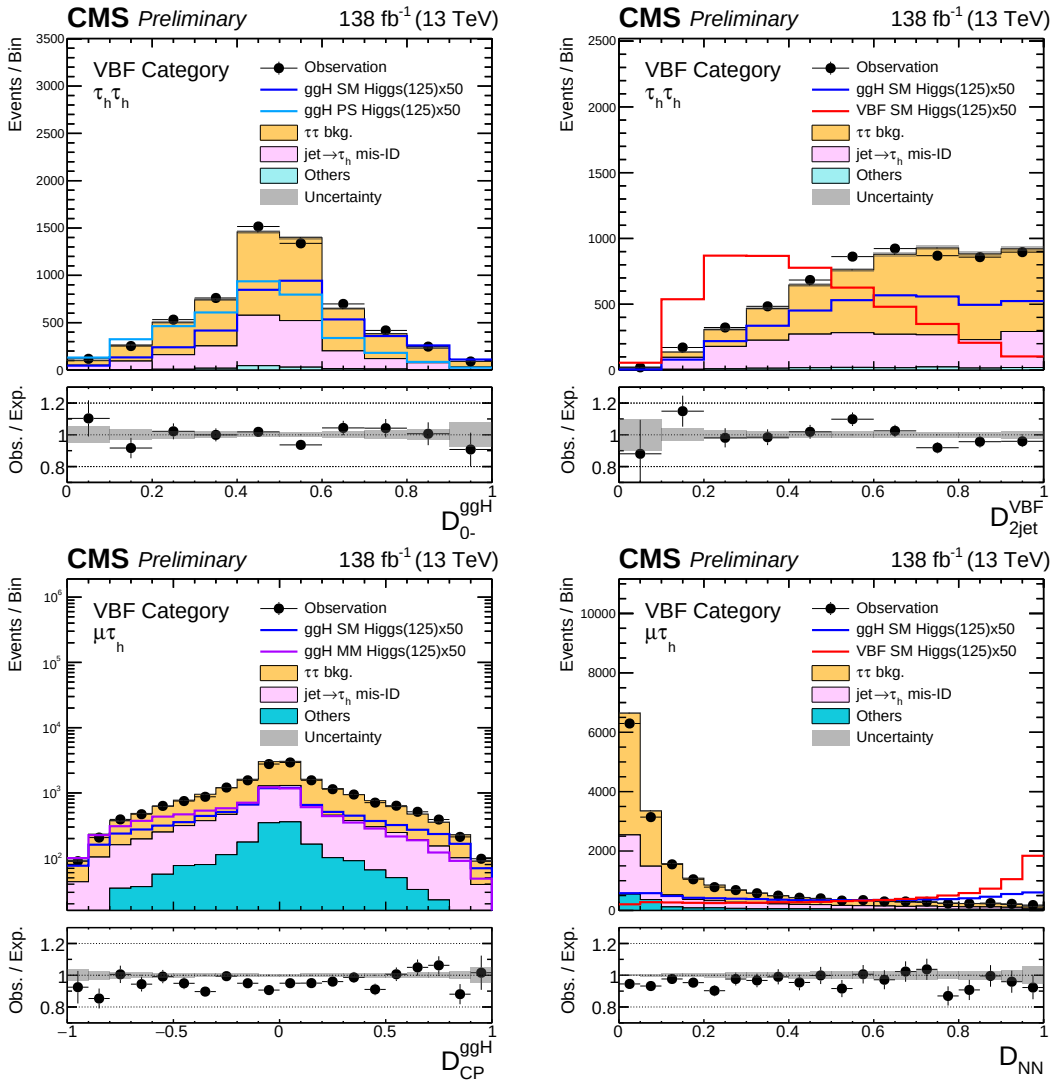

Figure 3: Examples of data and signal and background predictions for MELA and neural network discriminants in the $\tau_h\tau_h$ and $\mu\tau_h$ channels. Events passing the selections outlined in Section 5 and allocated to the VBF category are included. Only statistical uncertainties are shown. The expectation in the ratio plane is the sum of the estimated backgrounds and the SM H signal. For the $\mathcal{D}_{0-}^{ggH}$ discriminant the distribution expected for a pseudoscalar H is overlaid to be compared to the SM signal. Similarly, for the $\mathcal{D}_{CP}^{ggH}$ discriminant the distribution for a *CP*-violating scenario with maximum-mixing between *CP*-even and *CP*-odd couplings (labeled "MM" in the legend) is shown.

Table 5: List of observables used in the $\Delta\phi_{jj}$ method.

Category	Observable	Goal
0-jet	$m_{\tau\tau}$	Separate H signal from backgrounds
Boosted	$p_{\mathrm{T}}^{\tau\tau}$, $m_{\tau\tau}$	Separate H signal from backgrounds
VBF	$m_{\tau\tau}$	Separate H signal from backgrounds
VBF	$\Delta\phi_{jj}$	Differentiate between CP-even, CP-odd, and mixed CP scenarios

bin boundaries is the same for all channels and categories but we apply an additional merging of neighboring bins in cases where the statistical fluctuations in the signal or background templates are excessive.

8.3 Results of the ggH analysis

The results are extracted by performing a binned maximum likelihood fit to the data combining all categories for the different channels and data taking years. The likelihood function is defined as a product of conditional probabilities over all bins i:

$$\mathcal{L}(\mathrm{data}|\mu_{\mathrm{ggH}}, \mu_{\mathrm{qqH}}, \vec{f}, \theta) = \prod_i \mathrm{Poisson}(\mathrm{n_i}|s_i(\mu_{\mathrm{ggH}}, \mu_{\mathrm{qqH}}, \vec{f}, \theta) + b_i(\theta)) \cdot p(\tilde{\theta}|\theta), \tag{18}$$

where n_i is the observed number of data events in each bin. The signal and background expectations are given by s_i and b_i respectively, which are functions of θ, that represents the full set of nuisance parameters corresponding to the systematic uncertainties, and the parameters that modify the H signal processes: μ_{ggH}, μ_{qqH}, and $\vec{f}$. The parameters μ_{ggH} and μ_{qqH} are the H signal strength modifiers that respectively modify the ggH and VBF+VH cross sections with respect to the SM values. The $\vec{f}$ term represents the set of anomalous coupling parameters that modify the distributions of the ggH and/or VBF+VH signals. In the case of Hgg anomalous coupling measurements $\vec{f} = (f_{a3}^{\mathrm{ggH}}, f_{a3})$. Finally, the $p(\tilde{\theta}|\theta)$ term represents the full set of probability density functions (pdfs) of the uncertainties on the nominal values of the nuisance parameters $\tilde{\theta}$. The systematic uncertainties that affect only the normalizations of the signal and background processes are assigned log-normal pdfs, whereas the shape altering systematics are assigned Gaussian pdfs.

The negative log-likelihood is defined as

$$-2\Delta\ln\mathcal{L} = -2\Delta\ln\frac{\mathcal{L}(\mathrm{data}|\mu_{\mathrm{ggH}}, \mu_{\mathrm{qqH}}, \vec{f}, \theta)}{\mathcal{L}(\mathrm{data}|\hat{\mu}_{\mathrm{ggH}}, \hat{\mu}_{\mathrm{qqH}}, \hat{\vec{f}}, \hat{\theta})}, \tag{19}$$

with $\hat{\mu}_{\mathrm{ggH}}$, $\hat{\mu}_{\mathrm{qqH}}$, $\hat{\vec{f}}$, and $\hat{\theta}$ as the best-fit values of the signal modifiers and nuisance parameters. The 68% and 95% confidence intervals are identified when $-2\Delta\ln\mathcal{L} = 1.00$, and 3.84 respectively.

The measurement of f_{a3}^{ggH} (α^{Hff}) is performed using two methods based on MELA and $\Delta\phi_{jj}$, where the latter is used as a cross check of the former. An example of a pre-fit distribution for the MELA method is given in Fig. 4 for one of the most sensitive signal categories. Fig. 5 shows

the post-fit distribution in the VBF Tight-m_{jj} boosted category in the $\tau_h\tau_h$ channel, which is the most sensitive category used to extract the results using the $\Delta\phi_{jj}$ method. The results of the likelihood scans are shown in Fig. 6 (7) and listed in Table 6.

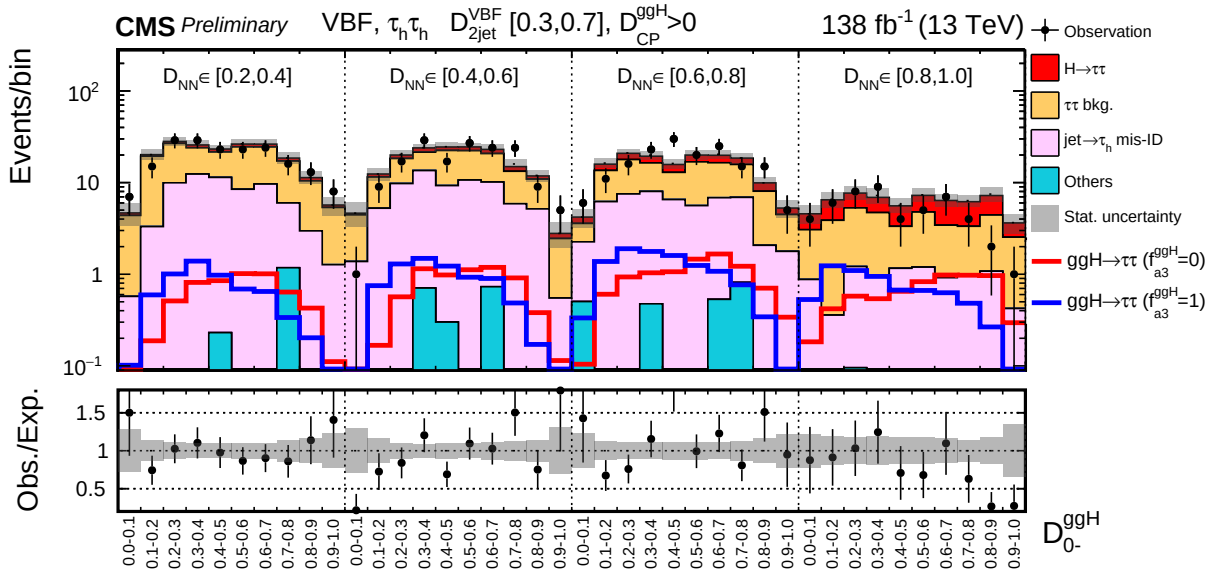

Figure 4: The observed and predicted 2D distribution of ($\mathcal{D}_{0-}^{\mathrm{ggH}}$, $\mathcal{D}_{\mathrm{NN}}$) before the fit to data in the most sensitive VBF category region with $0.3 < \mathcal{D}_{\mathrm{2jet}}^{\mathrm{VBF}} < 0.7$ in the $\tau_h\tau_h$ channel. The $\mathcal{D}_{\mathrm{CP}}^{\mathrm{ggH}} > 0$ bins are shown in the plots, and the $\mathcal{D}_{\mathrm{CP}}^{\mathrm{ggH}} < 0$ side has a symmetric distribution except for small fluctuations in the observed data. Only the statistical uncertainties are included in the uncertainty band.

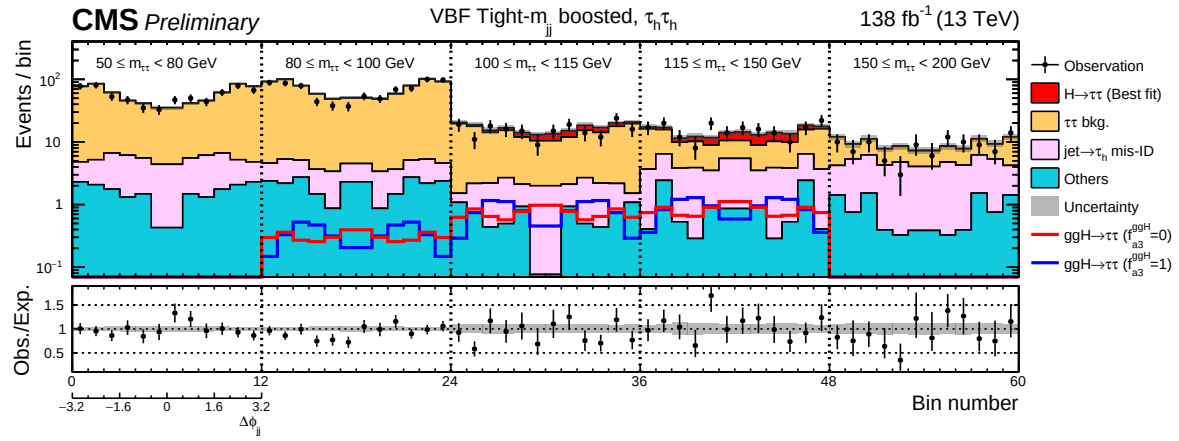

Figure 5: Observed and predicted 2D distributions after the fit to data in the VBF Tight-m_{jj} boosted category in the $\tau_h\tau_h$ channel. The uncertainty band accounts for all sources of systematic uncertainty on the signal and background predictions. The expectation in the ratio plane is the sum of the estimated backgrounds and the best fit signal.

For the MELA method, the maximum value of the $-2\Delta\ln\mathcal{L}$ is noticeably larger for the observed scan compared to the expected. We used pseudo-experiments to estimate the probability of obtaining a maximum value of the $-2\Delta\ln\mathcal{L}$ greater than or equal to the maximum

Table 6: Allowed 68% CL (central values with uncertainties) and 95% CL (in square brackets) intervals on anomalous ggH coupling parameters using the $H \to \tau\tau$ decay. The use of "-" indicates cases where no exclusion at the 95% CL was found. As indicated in the Table, the results are presented for the MELA method, as well as the $\Delta\phi_{jj}$ method for comparison. The final results of this study are from the MELA method.

Parameter	Method	Observed		Expected	
		68% CL	95% CL	68% CL	95% CL
f_{a3}^{ggH}	MELA	$0.08^{+0.35}_{-0.08}$	$[-0.09, 0.90]$	0.00 ± 0.36	-
f_{a3}^{ggH}	$\Delta\phi_{jj}$	$0.07^{+0.59}_{-0.19}$	-	0.00 ± 0.39	-
α^{Hff}	MELA	$11^{+18\circ}_{-10}$	$[-11, 63]$	$0 \pm 26^\circ$	-
α^{Hff}	$\Delta\phi_{jj}$	$10^{+32\circ}_{-24}$	-	$0 \pm 27^\circ$	-

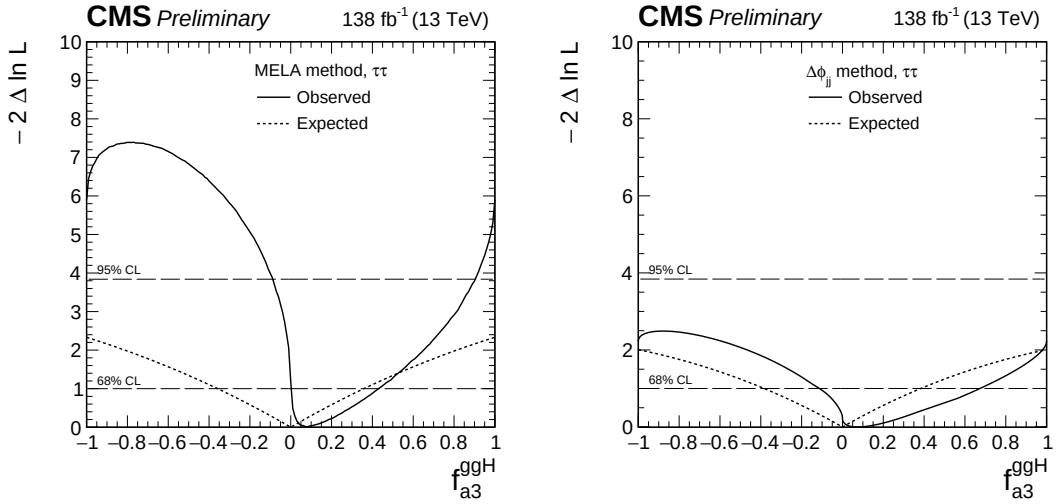

Figure 6: Observed (solid) and expected (dashed) likelihood scans of f_{a3}^{ggH} obtained with the MELA method (left) and the $\Delta\phi_{jj}$ method used as a cross check (right).

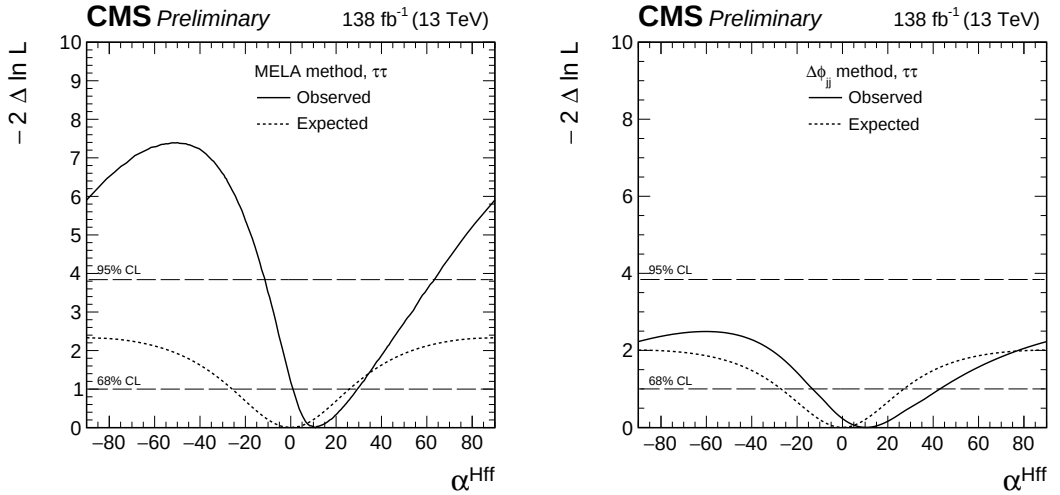

Figure 7: Observed (solid) and expected (dashed) likelihood scans of α^{Hff} obtained with the MELA method (left) and the $\Delta\phi_{jj}$ method used as a cross check (right).

$-2\Delta \ln \mathcal{L}$ of the observed scan. This probability was determined to be 33%. We thus conclude that the observed results are compatible with the signal plus background model.

The use of the MELA method is shown to improve the expected uncertainty on f_{a3}^{ggH} (α^{Hff}) by 13(7)%. This improvement owes partly to the use of neural networks that differentiate the H signal from the backgrounds more effectively, and partly to the inclusion of matrix-element discriminants that improve the separation between CP-even, CP-odd and mixed CP scenarios. In the case of the ggH production, the SM process is generated by the quark loop represented by the a_2^{gg} term in Eq. 1. This makes it harder to distinguish the anomalous a_3^{gg} contribution from the SM, as both are generated by dimension-six operators and many of their kinematic features are similar. Most of the sensitivity to CP-odd couplings is primarily in the azimuthal correlation of two jets, which explains why the full multivariate MELA treatment of kinematic information does not bring as much additional information as in the case of the VBF production, described in the following section, where the SM process is generated by the tree-level coupling g_1^{VV} in Eq. 1, which is a dimension-four operator. This leads to kinematic differences between the anomalous contributions and the SM in multiple observables and a much larger gain from the full multivariate MELA treatment.

We also cross-checked the results neglecting CP-odd contributions to the VBF and VH processes (f_{a3} fixed to zero). This was found to have only a minor effect on the best-fit value and uncertainty of f_{a3}^{ggH} (α^{Hff}). Therefore, we present results only for the more general case where f_{a3} is unconstrained.

9 Analysis of VBF and VH production

As MELA-based observables offer superior sensitivity and discrimination among different possible anomalous HVV couplings in the VBF and VH production compared to single kinematic observables, such as $\Delta\phi_{jj}$, the VBF study is conducted with MELA-based observables only. As sensitivity to VH anomalous effects is small with Run 2 statistics, the analysis is optimized for the VBF process.

Similar to the ggH analysis, we employ the same neural networks to separate VBF-like signal and background processes, while MELA discriminants offer optimal separation between different signal hypotheses (see Table 4). We use $\mathcal{D}_{\text{2jet}}^{\text{VBF}}$, defined in Eq. 14, to separate SM ggH production from the SM VBF production. Separate MELA discriminants, as defined in Eq. 20, are constructed to optimally separate the SM hypothesis from the potential anomalous coupling in the VBF production.

$$\begin{aligned} \mathcal{D}_{0-} &= \frac{\mathcal{P}_{\text{SM}}^{\text{VBF}}}{\mathcal{P}_{\text{SM}}^{\text{VBF}} + \mathcal{P}_{\text{PS}}^{\text{VBF}}} \quad \mathcal{D}_{0\text{h}+} = \frac{\mathcal{P}_{\text{SM}}^{\text{VBF}}}{\mathcal{P}_{\text{SM}}^{\text{VBF}} + \mathcal{P}_{\text{a2}}} \\ \mathcal{D}_{\Lambda 1} &= \frac{\mathcal{P}_{\text{SM}}^{\text{VBF}}}{\mathcal{P}_{\text{SM}}^{\text{VBF}} + \mathcal{P}_{\Lambda 1}} \quad \mathcal{D}_{\Lambda 1}^{\text{Z}\gamma} = \frac{\mathcal{P}_{\text{SM}}^{\text{VBF}}}{\mathcal{P}_{\text{SM}}^{\text{VBF}} + \mathcal{P}_{\Lambda 1}^{\text{Z}\gamma}} \end{aligned} \tag{20}$$

As for the Hgg analysis, we also define a pure CP-odd MELA discriminant $\mathcal{D}_{\text{CP}}^{\text{VBF}}$ in Eq. 21, that is sensitive to interference effects between the SM and pseudoscalar H hypotheses to directly probe for CP-violation in the HVV vertex:

$$\mathcal{D}_{\text{CP}}^{\text{VBF}} = \frac{\mathcal{P}_{\text{SM}-\text{PS}}^{\text{VBF}}}{\mathcal{P}_{\text{SM}}^{\text{VBF}} + \mathcal{P}_{\text{PS}}^{\text{VBF}}}. \tag{21}$$

The results of the VBF analysis are extracted with a global maximum likelihood fit based on 4D or 3D, 2D, and 1D distributions built in each of the VBF, Boosted, and 0-jet categories, respectively. The templates constructed for the Boosted and 0-jet categories are identical to those described for the ggH analysis in Section 8.1, although we note that in this case, in contrast to the former case, the chosen observables do provide some differentiation between anomalous coupling scenarios.

Depending on the anomalous coupling parameter being measured, we use three or four observables in total to construct our distributions in the VBF category. In all cases we include the $\mathcal{D}_{\text{NN}}$ and $\mathcal{D}_{\text{2jet}}^{\text{VBF}}$ observables. We additionally include $\mathcal{D}_{0-}$, $\mathcal{D}_{0\text{h}+}$, $\mathcal{D}_{\Lambda 1}$, and $\mathcal{D}_{\Lambda 1}^{\text{Z}\gamma}$, when we measure f_{a3}, f_{a2}, $f_{\Lambda 1}$, and $f_{\Lambda 1}^{\text{Z}\gamma}$, respectively; which we will collectively refer to as $\mathcal{D}_{\text{BSM}}$ in the following. The forth observable, which is included only for the measurement of the CP-odd parameter f_{a3}, is $\mathcal{D}_{\text{CP}}^{\text{VBF}}$. The selected events are binned into templates constructed using these observables.

The binning of the templates has been optimized following the criteria outlined in Section 8.1. For the $\ell\tau_{\text{h}}$ and $\tau_{\text{h}}\tau_{\text{h}}$ channels, we use 10, 8, and 4 equally sized bins for $\mathcal{D}_{\text{BSM}}$, $\mathcal{D}_{\text{NN}}$, and $\mathcal{D}_{\text{2jet}}^{\text{VBF}}$, respectively. For the eμ channel, we respectively use 3, 2, and 4 bins for these observables. In all cases we additionally check for bins where the total statistical uncertainty on the background prediction is in excess of 50%, and merge such bins with their neighbors. For the measurement of the f_{a3} parameter we include two bins in the $\mathcal{D}_{\text{CP}}^{\text{VBF}}$ discriminant, $\mathcal{D}_{\text{CP}}^{\text{VBF}} < 0$ and $\mathcal{D}_{\text{CP}}^{\text{VBF}} \geq 0$, to bring sensitivity to the sign of the interference between the CP-even and CP-odd contributions. The expected symmetry between these bins is enforced for the background and CP-conserving signal templates to reduce the influence of statistical fluctuations.

9.1 Results of the HVV analysis

The four f_{ai} parameters describing anomalous HVV couplings, as defined in Eqs. 1 and 3, are tested against the data according to the likelihood function defined in Eq. 18, following the same approach as that utilized in the analysis of the Hgg vertex.

An example of a pre-fit distribution in the most sensitive VBF category for the $\tau_h\tau_h$ channel is shown in Fig. 8. The results of the likelihood scans for Approaches 1 and 2 are shown in Figs. 9 and 10, respectively, and listed in Table 7. In each fit, the values of the other anomalous coupling parameters are set to zero, with the exception of the fit to the *CP*-odd parameter f_{a3}, which is extracted with f_{a3}^{ggH} left unconstrained. The signal strength parameters μ_{qqH} and μ_{ggH} are also profiled for all measurements. The best fit values of these parameters are consistent with unity.

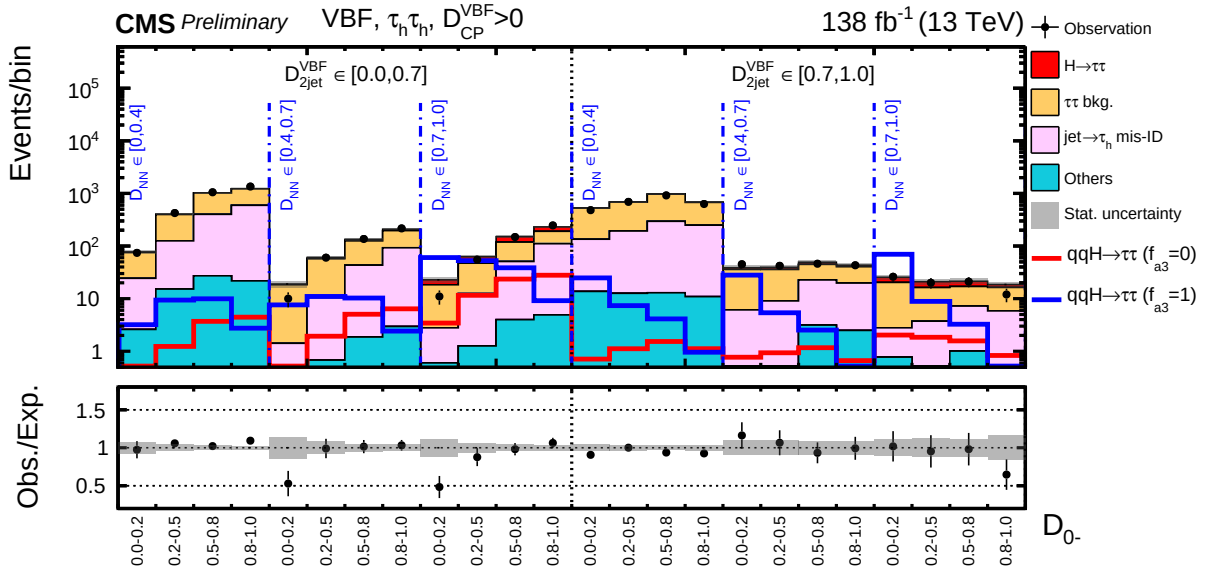

Figure 8: The observed and predicted 3D distribution of ($\mathcal{D}_{0-}$, $\mathcal{D}_{NN}$, $\mathcal{D}_{2jet}^{VBF}$) before the fit to data in the $\tau_h\tau_h$ channel for the most sensitive VBF category. The $\mathcal{D}_{CP}^{VBF} > 0$ bins are shown in the plots, and the $\mathcal{D}_{CP}^{VBF} < 0$ side has a symmetric distribution except for small fluctuation in the observations. Only the statistical uncertainties are included in the uncertainty band.

Table 7: Allowed 68% CL (central values with uncertainties) and 95% CL (in square brackets) intervals on anomalous HVV coupling parameters using the $H \to \tau\tau$ decay. Approaches 1 and 2 refer to the choice of the relationship between the a_i^{WW} and a_i^{ZZ} couplings, defined in Section 2.

Approach	Parameter	Observed/(10^{-3})		Expected/(10^{-3})	
		68% CL	95% CL	68% CL	95% CL
Approach 1	f_{a3}	$0.26^{+0.38}_{-0.21}$	$[-0.01, 1.30]$	0.00 ± 0.06	$[-0.23, 0.23]$
	f_{a2}	$1.1^{+0.9}_{-0.9} \cup [-1.8, -0.1]$	$[-3.4, 3.2]$	$0.0^{+0.6}_{-0.5}$	$[-1.4, 1.5]$
	$f_{\Lambda 1}$	$-0.12^{+0.08}_{-0.10}$	$[-0.34, 0.01]$	$0.00^{+0.19}_{-0.05}$	$[-0.15, 0.55]$
	$f_{\Lambda 1}^{Z\gamma}$	$2.5^{+1.8}_{-1.8}$	$[-3.6, 6.5]$	$0.0^{+1.5}_{-1.2}$	$[-3.2, 3.4]$
Approach 2	f_{a3}	$0.40^{+0.53}_{-0.33}$	$[-0.01, 1.90]$	0.00 ± 0.08	$[-0.33, 0.33]$

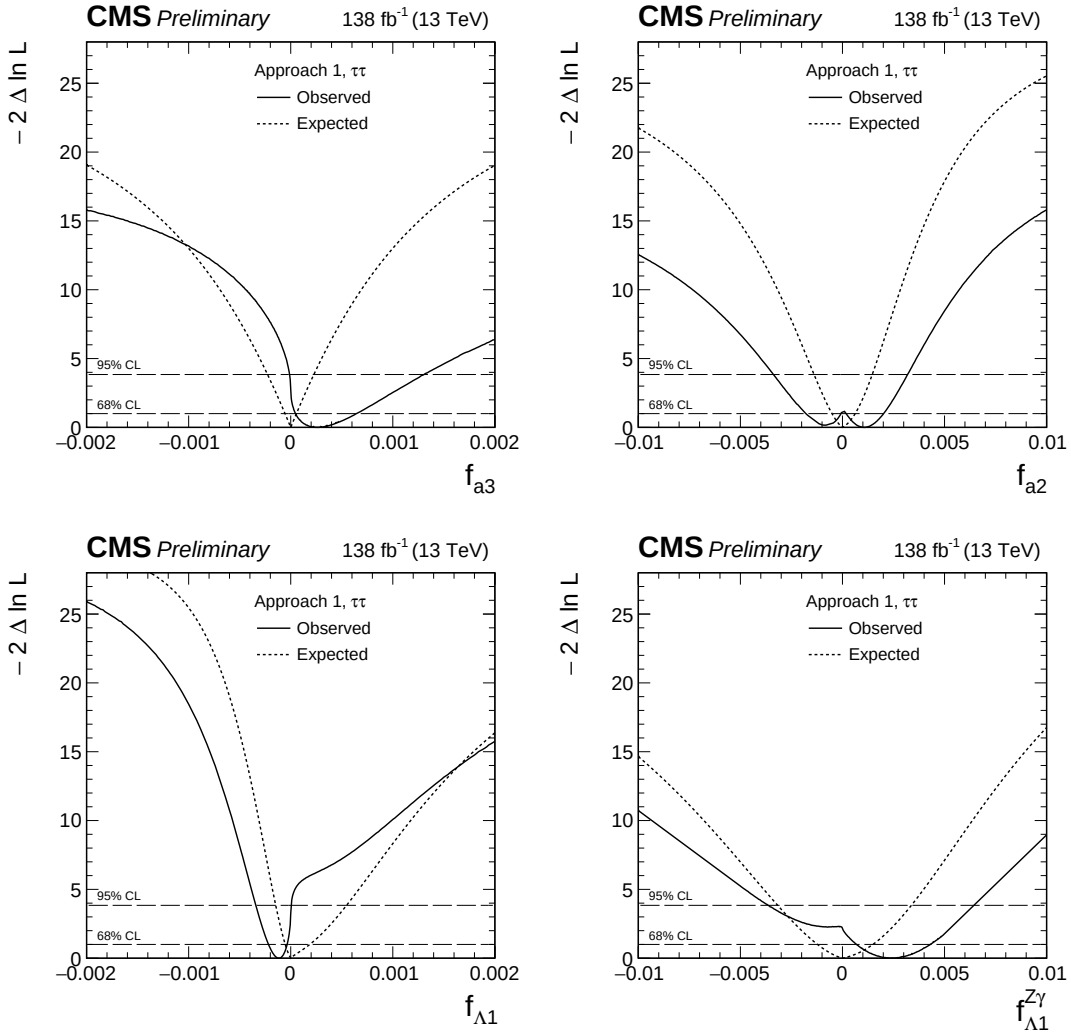

Figure 9: Observed (solid) and expected (dashed) likelihood scans of f_{a3} (top left), f_{a2} (top right), $f_{\Lambda 1}$ (bottom left), and $f_{\Lambda 1}^{Z\gamma}$ (bottom right) in Approach 1 ($a_i^{WW} = a_i^{ZZ}$).

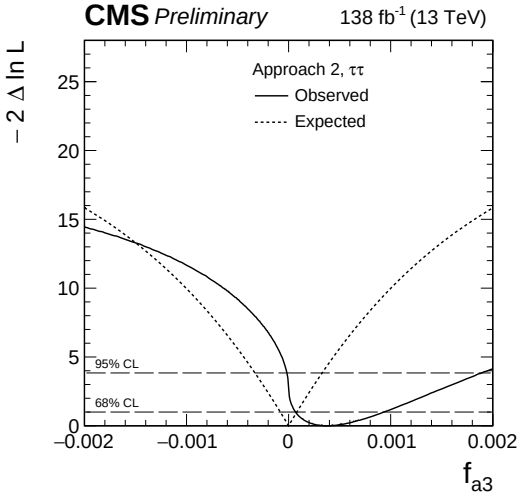

Figure 10: Observed (solid) and expected (dashed) likelihood scans of f_{a3} in Approach 2.

The presence of two minima in the observed likelihood scan for f_{a2} (and to a lesser extent $f_{\Lambda 1}^{Z\gamma}$) is a result of the limited sensitivity to the sign of the interference between the a_1 and a_2 ($\kappa_2^{Z\gamma}$) couplings, which is turn limits the sensitivity to the signs of the f_{a2} ($f_{\Lambda 1}^{Z\gamma}$) parameters.

The confidence level intervals on f_{ai} at 95% and 68% are more stringent compared to those utilizing the H decay information in the H $\to 4\ell$ channel [21] because VBF and VH production is sensitive to higher values of q_i^2 appearing in Eq. (1). Therefore, the cross section of anomalous contributions in VBF and VH production increases quickly with f_{ai}. As the cross section increases with respect to f_{ai} at different rates for production and decay, relatively small values of f_{ai} correspond to a substantial anomalous contribution to the production cross section. This leads to the plateau in the $-2\ln\mathcal{L}$ distributions for larger values of f_{ai} in Fig. 9. If we had used the cross section ratios for VBF production in the f_{ai} definition in Eq. (3), the appearance of the plateau and the narrow exclusion range would change. The f_{ai} constraints in Ref. [21] also utilize the VBF and VH production information, but the number of reconstructed H $\to 4\ell$ events in these production modes is still low compared to this analysis.

10 Combination of the results with other decay channels

The results of the anomalous coupling measurements presented in the previous sections can be further improved by combining with other H production/decay channels. The precision of the anomalous HVV and Hgg coupling measurements is improved by combining the $H \to \tau\tau$ and $H \to 4\ell$ decay channels, where we consider H production via VBF, VH, and ggH. We additionally constrain the anomalous Htt couplings by combining the $ggH \to \tau\tau/4\ell$ and $t\bar{t}H/tH \to \gamma\gamma/4\ell$ channels.

For all combinations, each H decay channel treats anomalous couplings in H production processes in the likelihood in a consistent manner. As with the $H \to \tau\tau$ channel-only fits, when we fit for a given parameter the values of the other anomalous couplings are set to zero with the exception of the fits to f_{a3} and f_{a3}^{ggH}, and the signal strength parameters are profiled in the combined likelihood fit. The number of signal strength parameters in the combined fit can be reduced by using a relationship between the production cross section ratios. For example, there are in principle four signal strength parameters for the combination of the $H \to \tau\tau$ and $H \to 4\ell$ channels ($\mu_{qqH}^{\tau\tau}$, $\mu_{ggH}^{\tau\tau}$, μ_{qqH}^{ZZ}, μ_{ggH}^{ZZ}). However, one degree of freedom is removed because the ratio between the ggH and VBF+VH cross sections is the same in both channels, $\mu_{qqH}^{\tau\tau}/\mu_{ggH}^{\tau\tau} = \mu_{qqH}^{ZZ}/\mu_{ggH}^{ZZ}$. Therefore, we can parameterize the combined fit with three signal strength parameters μ_{qqH}, μ_{ggH}, and η_τ, where η_τ stands for the relative strength of the H coupling to the τ leptons. For the combination with the $t\bar{t}H$ and tH results using the $H \to 4\ell$ and $H \to \gamma\gamma$ channels, the signal strengths $\mu_{t\bar{t}H}^{ZZ}$ and $\mu_{t\bar{t}H}^{\gamma\gamma}$ are not related for the f_{CP}^{Htt} measurement because they could differ by the loop involved in the $H \to \gamma\gamma$ decay. In the EFT approach, the fully-resolved loop parameterization following Ref. [40] is used to correlate them. All common systematic uncertainties are treated as being correlated between the channels in the combined likelihood fit.

The measurements of anomalous Hgg and HVV couplings using the MELA method are combined with the results using the on-shell $H \to 4\ell$ decay [21]. In the $H \to 4\ell$ analysis, anomalous HVV couplings can affect both production (VBF+VH) and decay ($H \to VV \to 4\ell$) processes. Information from both processes is taken into account in the analysis.

The combined likelihood scans for the HVV anomalous coupling measurements are shown in Figs. 11–12, and the allowed 68% CL and 95% CL intervals are listed in Table 8. The $H \to \tau\tau$ channel results mainly constrain small values of f_{ai} where the H production information is the dominant factor, whereas the $H \to 4\ell$ analysis provides major constraints at large values of f_{ai} based on the decay information.

The combined likelihood scans for the Hgg anomalous coupling measurements are shown in Fig. 13, and the allowed 68% CL and 95% CL intervals are listed in Table 9. The $H \to \tau\tau$ channel is more sensitive to f_{a3}^{ggH} than the $H \to 4\ell$ channel is, but there is a significant improvement from including both channels in the combination. Previous measurements by the CMS and ATLAS Collaborations [20, 21] were only able to differentiate between the *CP*-even and *CP*-odd scenarios with a significance slightly less than 1σ. With the current measurement, the pure *CP*-odd scenario is excluded with a significance in excess of 2σ for the first time.

Constraints on anomalous Htt couplings are obtained through the combination of the Hgg results with measurements of the $t\bar{t}H$ and tH processes in the $H \to 4\ell$ [21] and $H \to \gamma\gamma$ [22] channels. We measure the f_{CP}^{Htt} parameter by relating f_{a3}^{ggH} and f_{CP}^{Htt} as described in Eq. (10), under the assumption of top quark dominance in the gluon fusion loop. The results are presented in Fig. 13 and Table 9.

Table 8: Allowed 68% CL (central values with uncertainties) and 95% CL (in square brackets) intervals on anomalous HVV coupling parameters using the $H \to \tau\tau$ and $H \to 4\ell$ [21] decay channels, using two approaches described in Section 2 that define the relationship between the a_i^{WW} and a_i^{ZZ} couplings.

Approach	Parameter	Observed / (10^{-3})		Expected / (10^{-3})	
		68% CL	95% CL	68% CL	95% CL
Approach 1	f_{a3}	$0.20^{+0.26}_{-0.16}$	$[-0.01, 0.88]$	0.00 ± 0.05	$[-0.21, 0.21]$
	f_{a2}	$0.7^{+0.8}_{-0.6}$	$[-1.0, 2.5]$	$0.0^{+0.5}_{-0.4}$	$[-1.1, 1.2]$
	$f_{\Lambda 1}$	$-0.04^{+0.04}_{-0.08}$	$[-0.22, 0.16]$	$0.00^{+0.11}_{-0.04}$	$[-0.11, 0.38]$
	$f_{\Lambda 1}^{Z\gamma}$	$0.7^{+1.6}_{-1.3}$	$[-2.7, 4.1]$	$0.0^{+1.0}_{-1.0}$	$[-2.6, 2.5]$
Approach 2	f_{a3}	$0.28^{+0.39}_{-0.23}$	$[-0.01, 1.28]$	0.00 ± 0.08	$[-0.30, 0.30]$

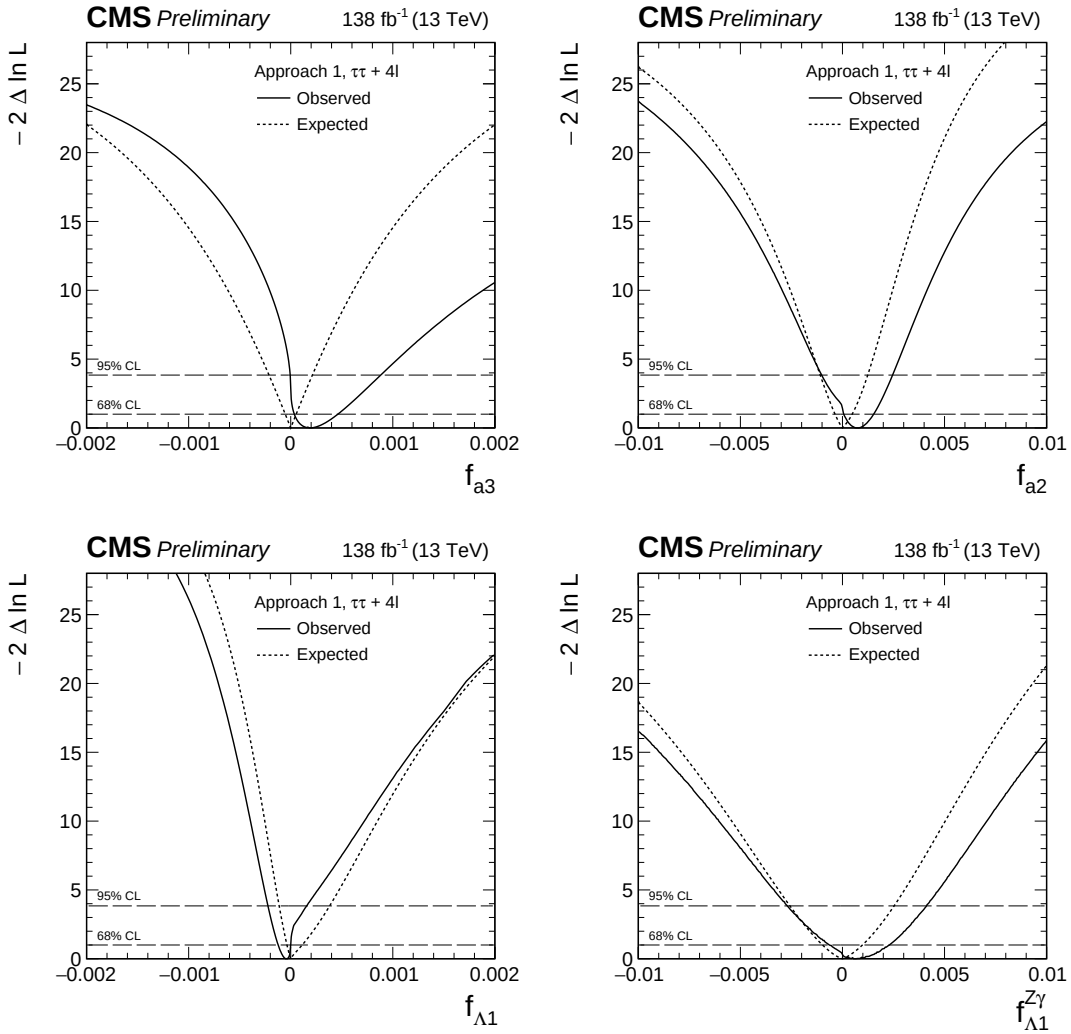

Figure 11: Observed (solid) and expected (dashed) likelihood scans of f_{a3} (top left), f_{a2} (top right), $f_{\Lambda 1}$ (bottom left), and $f_{\Lambda 1}^{Z\gamma}$ (bottom right) in Approach 1 ($a_i^{WW} = a_i^{ZZ}$) obtained with the combination of results using the $H \to \tau\tau$ and $H \to 4\ell$ [21] decay channels.

The combination of Hgg, $t\bar{t}H$, and tH results can be reinterpreted in the EFT approach as

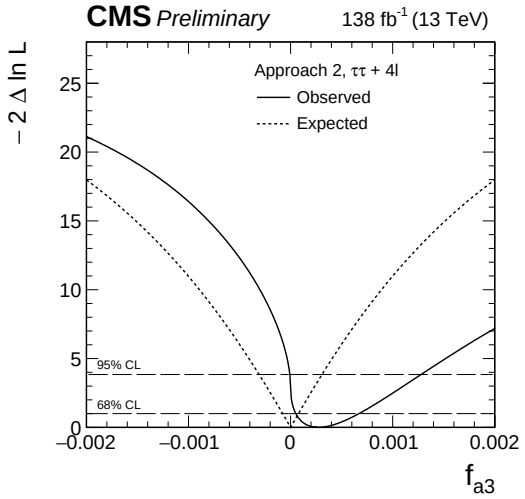

Figure 12: Observed (solid) and expected (dashed) likelihood scans of f_{a3} in Approach 2 (defined in Section 2) obtained with the combination of results using the $H \to \tau\tau$ and $H \to 4\ell$ [21] decay channels.

Table 9: Allowed 68% CL (central values with uncertainties) and 95% CL (in square brackets) intervals on f_{a3}^{ggH}, from the combination of the $H \to \tau\tau$ and $H \to 4\ell$ [21] decay channels, and f_{CP}^{Htt}, from the combination of the $H \to \tau\tau$, $H \to 4\ell$ [21], and $H \to \gamma\gamma$ [22] decay channels.

Parameter	Observed		Expected	
	68% CL	95% CL	68% CL	95% CL
f_{a3}^{ggH}	$0.07^{+0.32}_{-0.07}$	$[-0.15, 0.89]$	0.00 ± 0.26	-
f_{CP}^{Htt}	$0.03^{+0.17}_{-0.03}$	$[-0.07, 0.51]$	0.00 ± 0.12	$[-0.49, 0.49]$

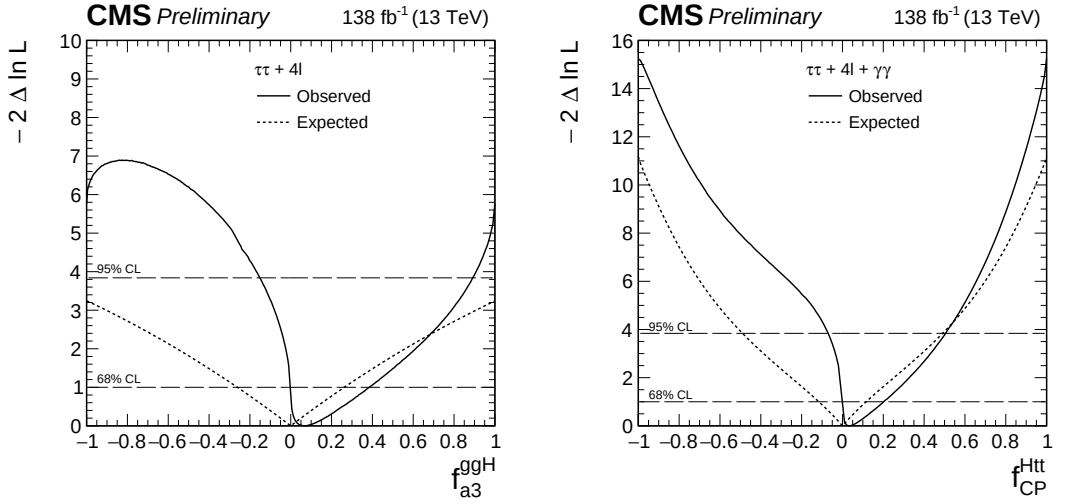

Figure 13: Left: the observed (solid) and expected (dashed) likelihood scans of f_{a3}^{ggH} and α^{Hff} obtained with the combination of results using the $H \to \tau\tau$ and $H \to 4\ell$ [21] decay channels. Right: The observed (solid) and expected (dashed) likelihood scans of f_{CP}^{Htt} obtained with the combination of results using the $H \to \tau\tau$, $H \to 4\ell$ [21], and $H \to \gamma\gamma$ [22] decay channels.

constraints on c_{gg} and $\tilde{c}_{gg}$. The likelihood scans for c_{gg} and $\tilde{c}_{gg}$ are performed with κ_t and $\tilde{\kappa}_t$ either profiled or fixed to SM expectation ($\kappa_t = 1$, $\tilde{\kappa}_t = 0$). The reinterpretation is presented in Fig. 14 and Table 10. We note that in both c_{gg} scans there is a second minimum away from $c_{gg} = 0$ due to the negative interference between the c_{gg} and κ_t contributions, as follows from Eq. (8).

Table 10: Allowed 68% CL (central values with uncertainties) and 95% CL (in square brackets) intervals on c_{gg} and $\tilde{c}_{gg}$ using the $H \to \tau\tau$, $H \to 4\ell$ [21], and $H \to \gamma\gamma$ [22] decay channels. Results are presented for two scenarios: κ_t and $\tilde{\kappa}_t$ profiled in the fit, and κ_t and $\tilde{\kappa}_t$ fixed to the SM expectation.

Parameter	Scenario		68% CL $/(10^{-2})$	95% CL $/(10^{-2})$
c_{gg}	Profiled	Observed	$-0.11^{+0.20}_{-0.26} \cup [-1.85, -1.42]$	$[-2.12, -1.35] \cup [-0.71, 0.36]$
		Expected	$0.00^{+0.18}_{-0.27} \cup [-1.91, -1.48]$	$[-2.23, 0.37]$
$\tilde{c}_{gg}$	Profiled	Observed	$0.00^{+1.29}_{-1.29}$	$[-1.79, 1.79]$
		Expected	0.00 ± 1.15	$[-1.78, 1.78]$
c_{gg}	Fixed	Observed	$-0.08^{+0.07}_{-0.15} \cup [-1.65, -1.54]$	$[-1.71, -1.54] \cup [-0.59, 0.05]$
		Expected	$0.00^{+0.06}_{-0.14} \cup [-1.73, -1.50]$	$[-1.78, 0.12]$
$\tilde{c}_{gg}$	Fixed	Observed	$0.22^{+0.28}_{-0.22} \cup [-0.50, 0.00]$	$[-0.74, 0.75]$
		Expected	0.00 ± 0.45	$[-0.87, 0.87]$

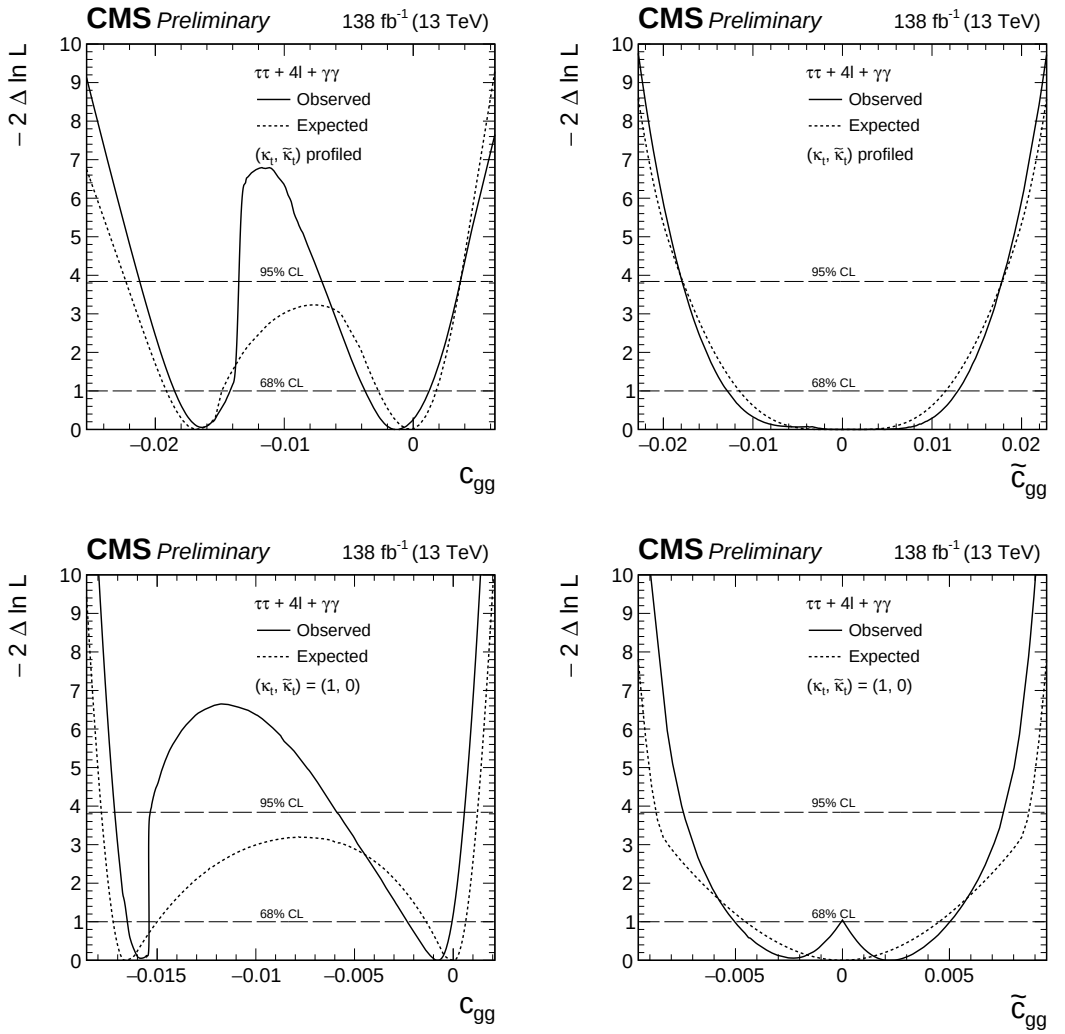

Figure 14: Observed (solid) and expected (dashed) likelihood scans of c_{gg} (left) and $\tilde{c}_{gg}$ (right) with κ_t and $\tilde{\kappa}_t$ profiled (top) and fixed to SM expectation (bottom) using the $H \to \tau\tau$, $H \to 4\ell$ [21], and $H \to \gamma\gamma$ [22] decay channels.

11 Summary

A study is presented of anomalous interactions of the H boson with vector bosons, including CP violation, using its associated production with two hadronic jets in gluon fusion, vector boson fusion, and associated production with a vector boson, and a subsequent decay to a pair of τ leptons. Constraints have been set on the CP violating effects in ggH production in terms of the effective cross section ratio f_{a3}^{ggH} and mixing angle α^{Hff} using both azimuthal correlations of the two leading hadronic jets in the events and matrix element techniques. Both methods yield comparable expected sensitivities and result in the most stringent limits on CP violation in ggH production followed by $\mathrm{H} \to \tau\tau$ decays to date. In the VBF and VH production analysis, constraints on the CP-violating parameter f_{a3} and on the CP-conserving parameters f_{a2}, $f_{\Lambda 1}$, and $f_{\Lambda 1}^{\mathrm{Z}\gamma}$ have been set using matrix element techniques. Further constraints were obtained in the combination of the $\mathrm{H} \to \tau\tau$, $\mathrm{H} \to 4\ell$, and $\mathrm{H} \to \gamma\gamma$ final states. The combination improves the limits on the anomalous coupling parameters typically by about 20–50%. The analysis excludes the pure CP-odd Hgg coupling scenario with a significance in excess of 2σ for the first time.

References

[1] ATLAS Collaboration, "Observation of a new particle in the search for the standard model Higgs boson with the ATLAS detector at the LHC", *Phys. Lett. B* **716** (2012) 1, doi:10.1016/j.physletb.2012.08.020, arXiv:1207.7214.

[2] CMS Collaboration, "Observation of a new boson at a mass of 125 GeV with the CMS experiment at the LHC", *Phys. Lett. B* **716** (2012) 30, doi:10.1016/j.physletb.2012.08.021, arXiv:1207.7235.

[3] CMS Collaboration, "Observation of a new boson with mass near 125 GeV in pp collisions at $\sqrt{s}$ = 7 and 8 TeV", *JHEP* **06** (2013) 081, doi:10.1007/JHEP06(2013)081, arXiv:1303.4571.

[4] S. L. Glashow, "Partial-symmetries of weak interactions", *Nucl. Phys.* **22** (1961) 579, doi:10.1016/0029-5582(61)90469-2.

[5] F. Englert and R. Brout, "Broken symmetry and the mass of gauge vector mesons", *Phys. Rev. Lett.* **13** (1964) 321, doi:10.1103/PhysRevLett.13.321.

[6] P. W. Higgs, "Broken symmetries, massless particles and gauge fields", *Phys. Lett.* **12** (1964) 132, doi:10.1016/0031-9163(64)91136-9.

[7] P. W. Higgs, "Broken symmetries and the masses of gauge bosons", *Phys. Rev. Lett.* **13** (1964) 508, doi:10.1103/PhysRevLett.13.508.

[8] G. S. Guralnik, C. R. Hagen, and T. W. B. Kibble, "Global conservation laws and massless particles", *Phys. Rev. Lett.* **13** (1964) 585, doi:10.1103/PhysRevLett.13.585.

[9] S. Weinberg, "A model of leptons", *Phys. Rev. Lett.* **19** (1967) 1264, doi:10.1103/PhysRevLett.19.1264.

[10] A. Salam, "Weak and electromagnetic interactions", *Conf. Proc. C* **680519** (1968) 367, doi:10.1142/9789812795915_0034.

[11] CMS Collaboration, "Constraints on the spin-parity and anomalous HVV couplings of the Higgs boson in proton collisions at 7 and 8 TeV", *Phys. Rev. D* **92** (2015) 012004, doi:10.1103/PhysRevD.92.012004, arXiv:1411.3441.

[12] ATLAS Collaboration, "Study of the spin and parity of the Higgs boson in diboson decays with the ATLAS detector", *Eur. Phys. J. C* **75** (2015) 476, doi:10.1140/epjc/s10052-015-3685-1, arXiv:1506.05669.

[13] CMS Collaboration, "Study of the mass and spin-parity of the Higgs boson candidate via its decays to Z boson pairs", *Phys. Rev. Lett.* **110** (2013) 081803, doi:10.1103/PhysRevLett.110.081803, arXiv:1212.6639.

[14] CMS Collaboration, "Measurement of the properties of a Higgs boson in the four-lepton final state", *Phys. Rev. D* **89** (2014) 092007, doi:10.1103/PhysRevD.89.092007, arXiv:1312.5353.

[15] CMS Collaboration, "Limits on the Higgs boson lifetime and width from its decay to four charged leptons", *Phys. Rev. D* **92** (2015) 072010, doi:10.1103/PhysRevD.92.072010, arXiv:1507.06656.

[16] CMS Collaboration, "Combined search for anomalous pseudoscalar HVV couplings in VH(H $\to$ b$\bar{\text{b}}$) production and H $\to$ VV decay", *Phys. Lett. B* **759** (2016) 672, doi:10.1016/j.physletb.2016.06.004, arXiv:1602.04305.

[17] CMS Collaboration, "Constraints on anomalous Higgs boson couplings using production and decay information in the four-lepton final state", *Phys. Lett. B* **775** (2017) 1, doi:10.1016/j.physletb.2017.10.021, arXiv:1707.00541.

[18] CMS Collaboration, "Measurements of the Higgs boson width and anomalous HVV couplings from on-shell and off-shell production in the four-lepton final state", *Phys. Rev. D* **99** (2019) 112003, doi:10.1103/PhysRevD.99.112003, arXiv:1901.00174.

[19] CMS Collaboration, "Constraints on anomalous HVV couplings from the production of Higgs bosons decaying to τ lepton pairs", *Phys. Rev. D* **100** (2019) 112002, doi:10.1103/PhysRevD.100.112002, arXiv:1903.06973.

[20] ATLAS Collaboration, "Constraints on Higgs boson properties using WW$^*(\to \mathrm{e}\nu\mu\nu)jj$ production in 36.1 fb^{-1} of $\sqrt{s}$=13 TeV pp collisions with the ATLAS detector", (2021). arXiv:2109.13808. Submitted to *Eur. Phys. J. C*.

[21] CMS Collaboration, "Constraints on anomalous Higgs boson couplings to vector bosons and fermions in its production and decay using the four-lepton final state", *Phys. Rev. D* **104** (2021) 052004, doi:10.1103/PhysRevD.104.052004, arXiv:2104.12152.

[22] CMS Collaboration, "Measurements of t$\bar{\text{t}}$H production and the CP structure of the Yukawa interaction between the Higgs boson and top quark in the diphoton decay channel", *Phys. Rev. Lett.* **125** (2020) 061801, doi:10.1103/PhysRevLett.125.061801, arXiv:2003.10866.

[23] ATLAS Collaboration, "CP properties of Higgs boson interactions with top quarks in the $t\bar{t}H$ and tH processes using $H \to \gamma\gamma$ with the ATLAS detector", *Phys. Rev. Lett.* **125** (2020) 061802, doi:10.1103/PhysRevLett.125.061802, arXiv:2004.04545.

[24] Y. Gao et al., "Spin determination of single-produced resonances at hadron colliders", *Phys. Rev. D* **81** (2010) 075022, doi:10.1103/PhysRevD.81.075022, arXiv:1001.3396.

[25] S. Bolognesi et al., "Spin and parity of a single-produced resonance at the LHC", *Phys. Rev. D* **86** (2012) 095031, doi:10.1103/PhysRevD.86.095031, arXiv:1208.4018.

[26] I. Anderson et al., "Constraining anomalous HVV interactions at proton and lepton colliders", *Phys. Rev. D* **89** (2014) 035007, doi:10.1103/PhysRevD.89.035007, arXiv:1309.4819.

[27] A. V. Gritsan, R. Röntsch, M. Schulze, and M. Xiao, "Constraining anomalous Higgs boson couplings to the heavy flavor fermions using matrix element techniques", *Phys. Rev. D* **94** (2016) 055023, doi:10.1103/PhysRevD.94.055023, arXiv:1606.03107.

[28] F. Chollet et al., "Keras". https://keras.io, 2015.

[29] T. Plehn, D. L. Rainwater, and D. Zeppenfeld, "Determining the structure of Higgs couplings at the LHC", *Phys. Rev. Lett.* **88** (2002) 051801, doi:10.1103/PhysRevLett.88.051801, arXiv:hep-ph/0105325.

[30] V. Hankele, G. Klamke, D. Zeppenfeld, and T. Figy, "Anomalous Higgs boson couplings in vector boson fusion at the CERN LHC", *Phys. Rev. D* **74** (2006) 095001, doi:10.1103/PhysRevD.74.095001, arXiv:hep-ph/0609075.

[31] E. Accomando et al., "Workshop on CP studies and non-standard Higgs physics", (2006). arXiv:hep-ph/0608079.

[32] K. Hagiwara, Q. Li, and K. Mawatari, "Jet angular correlation in vector-boson fusion processes at hadron colliders", *JHEP* **07** (2009) 101, doi:10.1088/1126-6708/2009/07/101, arXiv:0905.4314.

[33] A. De Rújula et al., "Higgs look-alikes at the LHC", *Phys. Rev. D* **82** (2010) 013003, doi:10.1103/PhysRevD.82.013003, arXiv:1001.5300.

[34] J. Ellis, D. S. Hwang, V. Sanz, and T. You, "A fast track towards the 'Higgs' spin and parity", *JHEP* **11** (2012) 134, doi:10.1007/JHEP11(2012)134, arXiv:1208.6002.

[35] P. Artoisenet et al., "A framework for Higgs characterisation", *JHEP* **11** (2013) 043, doi:10.1007/JHEP11(2013)043, arXiv:1306.6464.

[36] M. J. Dolan, P. Harris, M. Jankowiak, and M. Spannowsky, "Constraining CP-violating Higgs sectors at the LHC using gluon fusion", *Phys. Rev. D* **90** (2014) 073008, doi:10.1103/PhysRevD.90.073008, arXiv:1406.3322.

[37] A. Greljo, G. Isidori, J. M. Lindert, and D. Marzocca, "Pseudo-observables in electroweak Higgs production", *Eur. Phys. J. C* **76** (2016) 158, doi:10.1140/epjc/s10052-016-4000-5, arXiv:1512.06135.

[38] A. V. Gritsan et al., "New features in the JHU generator framework: constraining Higgs boson properties from on-shell and off-shell production", *Phys. Rev. D* **102** (2020) 056022, doi:10.1103/PhysRevD.102.056022, arXiv:2002.09888.

[39] LHC Higgs Cross Section Working Group, "Handbook of LHC Higgs cross sections: 4. deciphering the nature of the Higgs sector", *CERN* (2016) doi:10.23731/CYRM-2017-002, arXiv:1610.07922.

[40] J. Davis et al., "Constraining anomalous Higgs boson couplings to virtual photons", (2021). arXiv:2109.13363.

[41] ATLAS Collaboration, "Evidence for the spin-0 nature of the Higgs boson using ATLAS data", *Phys. Lett. B* **726** (2013) 120, doi:10.1016/j.physletb.2013.08.026, arXiv:1307.1432.

[42] ATLAS Collaboration, "Test of CP invariance in vector-boson fusion production of the Higgs boson using the optimal observable method in the ditau decay channel with the ATLAS detector", *Eur. Phys. J. C* **76** (2016) 658, doi:10.1140/epjc/s10052-016-4499-5, arXiv:1602.04516.

[43] ATLAS Collaboration, "Measurement of inclusive and differential cross sections in the $H \to ZZ^* \to 4\ell$ decay channel in pp collisions at $\sqrt{s} = 13$ TeV with the ATLAS detector", *JHEP* **10** (2017) 132, doi:10.1007/JHEP10(2017)132, arXiv:1708.02810.

[44] ATLAS Collaboration, "Measurement of the Higgs boson coupling properties in the $H \to ZZ^* \to 4\ell$ decay channel at $\sqrt{s}$ = 13 TeV with the ATLAS detector", *JHEP* **03** (2018) 095, doi:10.1007/JHEP03(2018)095, arXiv:1712.02304.

[45] ATLAS Collaboration, "Measurements of Higgs boson properties in the diphoton decay channel with 36 fb^{-1} of pp collision data at $\sqrt{s} = 13$ TeV with the ATLAS detector", *Phys. Rev. D* **98** (2018) 052005, doi:10.1103/PhysRevD.98.052005, arXiv:1802.04146.

[46] ATLAS Collaboration, "Test of CP invariance in vector-boson fusion production of the Higgs boson in the $H \to \tau\tau$ channel in proton−proton collisions at $\sqrt{s}$ = 13 TeV with the ATLAS detector", *Phys. Lett. B* **805** (2020) 135426, doi:10.1016/j.physletb.2020.135426, arXiv:2002.05315.

[47] G. Klamke and D. Zeppenfeld, "Higgs plus two jet production via gluon fusion as a signal at the CERN LHC", *JHEP* **04** (2007) 052, doi:10.1088/1126-6708/2007/04/052, arXiv:hep-ph/0703202.

[48] CMS Collaboration, "The CMS trigger system", *JINST* **12** (2017) P01020, doi:10.1088/1748-0221/12/01/P01020, arXiv:1609.02366.

[49] CMS Collaboration, "The CMS experiment at the CERN LHC", *JINST* **3** (2008) S08004, doi:10.1088/1748-0221/3/08/S08004.

[50] CMS Collaboration, "Precision luminosity measurement in proton-proton collisions at $\sqrt{s} = 13$ TeV in 2015 and 2016 at CMS", *Eur. Phys. J. C* **81** (2021) 800, doi:10.1140/epjc/s10052-021-09538-2, arXiv:2104.01927.

[51] CMS Collaboration, "CMS luminosity measurement for the 2017 data-taking period at $\sqrt{s} = 13$ TeV", CMS Physics Analysis Summary CMS-PAS-LUM-17-004, 2018.

[52] CMS Collaboration, "CMS luminosity measurement for the 2018 data-taking period at $\sqrt{s} = 13$ TeV", CMS Physics Analysis Summary CMS-PAS-LUM-18-002, 2019.

[53] T. Sjostrand et al., "An introduction to PYTHIA 8.2", *Comput. Phys. Commun.* **191** (2015) 159, doi:10.1016/j.cpc.2015.01.024, arXiv:1410.3012.

[54] CMS Collaboration, "Event generator tunes obtained from underlying event and multiparton scattering measurements", *Eur. Phys. J. C* **76** (2016) 155, doi:10.1140/epjc/s10052-016-3988-x, arXiv:1512.00815.

[55] CMS Collaboration, "Extraction and validation of a new set of CMS PYTHIA8 tunes from underlying-event measurements", *Eur. Phys. J. C* **80** (2020) 4, doi:10.1140/epjc/s10052-019-7499-4, arXiv:1903.12179.

[56] NNPDF Collaboration, "Parton distributions for the LHC Run II", *JHEP* **04** (2015) 040, doi:10.1007/JHEP04(2015)040, arXiv:1410.8849.

[57] NNPDF Collaboration, "Parton distributions from high-precision collider data", *Eur. Phys. J. C* **77** (2017) 663, doi:10.1140/epjc/s10052-017-5199-5, arXiv:1706.00428.

[58] GEANT4 Collaboration, "GEANT4—a simulation toolkit", *Nucl. Instrum. Meth. A* **506** (2003) 250, doi:10.1016/S0168-9002(03)01368-8.

[59] P. Nason, "A new method for combining NLO QCD with shower Monte Carlo algorithms", *JHEP* **11** (2004) 040, doi:10.1088/1126-6708/2004/11/040, arXiv:hep-ph/0409146.

[60] S. Frixione, P. Nason, and C. Oleari, "Matching NLO QCD computations with parton shower simulations: the POWHEG method", *JHEP* **11** (2007) 070, doi:10.1088/1126-6708/2007/11/070, arXiv:0709.2092.

[61] S. Alioli, P. Nason, C. Oleari, and E. Re, "A general framework for implementing NLO calculations in shower Monte Carlo programs: the POWHEG BOX", *JHEP* **06** (2010) 043, doi:10.1007/JHEP06(2010)043, arXiv:1002.2581.

[62] P. Nason and C. Oleari, "NLO Higgs boson production via vector-boson fusion matched with shower in POWHEG", *JHEP* **02** (2010) 037, doi:10.1007/JHEP02(2010)037, arXiv:0911.5299.

[63] T. Ježo and P. Nason, "On the Treatment of Resonances in Next-to-Leading Order Calculations Matched to a Parton Shower", *JHEP* **12** (2015) 065, doi:10.1007/JHEP12(2015)065, arXiv:1509.09071.

[64] F. Granata, J. M. Lindert, C. Oleari, and S. Pozzorini, "NLO QCD+EW predictions for HV and HV +jet production including parton-shower effects", *JHEP* **09** (2017) 012, doi:10.1007/JHEP09(2017)012, arXiv:1706.03522.

[65] J. Alwall et al., "The automated computation of tree-level and next-to-leading order differential cross sections, and their matching to parton shower simulations", *JHEP* **07** (2014) 079, doi:10.1007/JHEP07(2014)079, arXiv:1405.0301.

[66] R. Frederix and S. Frixione, "Merging meets matching in MC@NLO", *JHEP* **12** (2012) 061, doi:10.1007/JHEP12(2012)061, arXiv:1209.6215.

[67] F. Demartin et al., "Higgs characterisation at NLO in QCD: CP properties of the top-quark Yukawa interaction", *Eur. Phys. J.* **C74** (2014) 3065, doi:10.1140/epjc/s10052-014-3065-2, arXiv:1407.5089.

[68] K. Hamilton, P. Nason, E. Re, and G. Zanderighi, "NNLOPS simulation of Higgs boson production", *JHEP* **10** (2013) 222, doi:10.1007/JHEP10(2013)222, arXiv:1309.0017.

[69] K. Hamilton, P. Nason, and G. Zanderighi, "Finite quark-mass effects in the NNLOPS POWHEG+MiNLO Higgs generator", *JHEP* **05** (2015) 140, doi:10.1007/JHEP05(2015)140, arXiv:1501.04637.

[70] J. Alwall et al., "Comparative study of various algorithms for the merging of parton showers and matrix elements in hadronic collisions", *Eur. Phys. J. C* **53** (2008) 473, doi:10.1140/epjc/s10052-007-0490-5, arXiv:0706.2569.

[71] S. Alioli, S.-O. Moch, and P. Uwer, "Hadronic top-quark pair-production with one jet and parton showering", *JHEP* **01** (2012) 137, doi:10.1007/JHEP01(2012)137, arXiv:1110.5251.

[72] R. Frederix, E. Re, and P. Torrielli, "Single-top t-channel hadroproduction in the four-flavour scheme with POWHEG and aMC@NLO", *JHEP* **09** (2012) 130, doi:10.1007/JHEP09(2012)130, arXiv:1207.5391.

[73] E. Re, "Single-top Wt-channel production matched with parton showers using the POWHEG method", *Eur. Phys. J. C* **71** (2011) 1547, doi:10.1140/epjc/s10052-011-1547-z, arXiv:1009.2450.

[74] CMS Collaboration, "Particle-flow reconstruction and global event description with the CMS detector", *JINST* **12** (2017) P10003, doi:10.1088/1748-0221/12/10/P10003, arXiv:1706.04965.

[75] M. Cacciari, G. P. Salam, and G. Soyez, "The anti-k_{T} jet clustering algorithm", *JHEP* **04** (2008) 063, doi:10.1088/1126-6708/2008/04/063, arXiv:0802.1189.

[76] M. Cacciari, G. P. Salam, and G. Soyez, "FastJet user manual", *Eur. Phys. J. C* **72** (2012) 1896, doi:10.1140/epjc/s10052-012-1896-2, arXiv:1111.6097.

[77] CMS Collaboration, "Performance of electron reconstruction and selection with the CMS detector in proton-proton collisions at $\sqrt{s} = 8$ TeV", *JINST* **10** (2015) P06005, doi:10.1088/1748-0221/10/06/P06005, arXiv:1502.02701.

[78] CMS Collaboration, "Performance of the CMS muon detector and muon reconstruction with proton-proton collisons at $\sqrt{s} = 13$ TeV", *JINST* **13** (2018) P06015, doi:10.1088/1748-0221/13/06/P06015, arXiv:1804.04528.

[79] M. Cacciari, G. P. Salam, "Dispelling the N^3 myth for the k_t jet-finder", *Phys. Lett. B* **641** (2006) 57, doi:10.1016/j.physletb.2006.08.037, arXiv:hep-ph/0512210.

[80] CMS Collaboration, "Identification of heavy-flavour jets with the CMS detector in pp collisions at 13 TeV", *JINST* **13** (2018) P05011, doi:10.1088/1748-0221/13/05/P05011, arXiv:1712.07158.

[81] CMS Collaboration, "Reconstruction and identification of τ lepton decays to hadrons and ν_τ at CMS", *JINST* **11** (2016) P01019, doi:10.1088/1748-0221/11/01/P01019, arXiv:1510.07488.

[82] CMS Collaboration, "Performance of reconstruction and identification of τ leptons decaying to hadrons and ν_τ in pp collisions at $\sqrt{s} = 13$ TeV", *JINST* **13** (2018) P10005, doi:10.1088/1748-0221/13/10/P10005, arXiv:1809.02816.

[83] CMS Collaboration, "Performance of the DeepTau algorithm for the discrimination of taus against jets, electron, and muons", CMS Detector Performance Note CMS-DP-2019-033, 2019.

[84] CMS Collaboration, "Performance of missing transverse momentum in pp collisions at $\sqrt{s} = 13$ TeV using the CMS detector", CMS Physics Analysis Summary CMS-PAS-JME-17-001, 2018.

[85] L. Bianchini, J. Conway, E. K. Friis, and C. Veelken, "Reconstruction of the Higgs mass in $H \to \tau\tau$ events by dynamical likelihood techniques", *J. Phys. Conf. Ser.* **513** (2014) 022035, doi:10.1088/1742-6596/513/2/022035.

[86] D. Jang, "Search for MSSM Higgs decaying to τ pairs in $p\bar{p}$ collision at $\sqrt{s}$ = 1.96 TeV at CDF". PhD thesis, Rutgers U., Piscataway, 2006. doi:10.2172/892378.

[87] CMS Collaboration, "Observation of the Higgs boson decay to a pair of τ leptons with the CMS detector", *Phys. Lett. B* **779** (2018) 283, doi:10.1016/j.physletb.2018.02.004, arXiv:1708.00373.

[88] CMS Collaboration, "An embedding technique to determine $\tau\tau$ backgrounds in proton-proton collision data", *JINST* **14** (2019) P06032, doi:10.1088/1748-0221/14/06/p06032, arXiv:1903.01216.

[89] CMS Collaboration, "Measurement of the $Z\gamma^* \to \tau\tau$ cross section in pp collisions at $\sqrt{s} = 13$ TeV and validation of τ lepton analysis techniques", *Eur. Phys. J. C* **78** (2018) 708, doi:10.1140/epjc/s10052-018-6146-9, arXiv:1801.03535.

[90] CMS Collaboration, "Measurement of the differential cross section for top quark pair production in pp collisions at $\sqrt{s} = 8$ TeV", *Eur. Phys. J. C* **75** (2015) 542, doi:10.1140/epjc/s10052-015-3709-x, arXiv:1505.04480.

[91] V. Hankele, G. Klamke, and D. Zeppenfeld, "Higgs + 2 jets as a probe for CP properties", (2006). arXiv:hep-ph/0605117.